

Synthetic aperture radar imaging of submarine manifestations on sea surface with different acquisition strategies using a novel revamped velocity bunching modulation mechanism

Arivazhagan S, Shanmuga Sundari Mariappan, M MaryRosaline Tamil Selvi & Rajesh Killampalli

To cite this article: Arivazhagan S, Shanmuga Sundari Mariappan, M MaryRosaline Tamil Selvi & Rajesh Killampalli (2025) Synthetic aperture radar imaging of submarine manifestations on sea surface with different acquisition strategies using a novel revamped velocity bunching modulation mechanism, International Journal of Remote Sensing, 46:22, 8567-8613, DOI: [10.1080/01431161.2025.2571232](https://doi.org/10.1080/01431161.2025.2571232)

To link to this article: <https://doi.org/10.1080/01431161.2025.2571232>



Published online: 17 Oct 2025.



Submit your article to this journal [↗](#)



Article views: 61



View related articles [↗](#)



View Crossmark data [↗](#)



Synthetic aperture radar imaging of submarine manifestations on sea surface with different acquisition strategies using a novel revamped velocity bunching modulation mechanism

Arivazhagan S^a, Shanmuga Sundari Mariappan^a, M MaryRosaline Tamil Selvi^{id}^a and Rajesh Killampalli^b

^aDepartment of Electronics and Communication Engineering, Mepco Schlenk Engineering College, Sivakasi, India; ^bCentre for Atmospheric Sciences, Indian Institute of Technology, Delhi, India

ABSTRACT

Detection and localization of submarine wakes from synthetic aperture radar images is one of the potential resources for oceanic surveillance. It is challenging to access all real-time SAR images of submarine wakes. Therefore, modelling them is necessary to construct the dataset for detecting submarine wakes using cutting-edge deep learning technologies. This study intends to design an SAR image simulator system that models the SAR imaging of submarine trails considering eclectic sea state conditions, submarine parameters, and radar-looking scenarios. Here, a novel revamped velocity bunching mechanism (RVBM) is adopted to simulate both single- and multi-look SAR images by incorporating the Kaiser-Bessel weighting function. This study simulates the perturbation experienced by the three Indian classes of submarines (Sindhughosh, Kalvari, and Shishumar) on SAR images in the Indian Ocean and Mediterranean Sea regions. The trustworthiness of the proposed SAR image simulator has been confirmed by comparing the results with six independent Sentinel-1 SAR images using a variety of qualitative and quantitative measures.

ARTICLE HISTORY

Received 24 May 2025

Accepted 30 September 2025

KEYWORDS

Submarine wakes; SAR imaging; RVBM; WW3; MATLAB

1. Introduction

Maritime Domain Awareness (MDA) is essential for ensuring the nation's maritime safety, security, and sustainability. MDA involves collecting, integrating, and interpreting data from various sources to track the vessels and detect illicit activities. Marine remote sensing encompasses both aerial and satellite-based approaches for collecting data regarding the ocean surface. Synthetic Aperture Radar (SAR) has grown into a cornerstone in oceanographic research due to its weather resiliency and perpetual accessibility. In 1951, Carl A. Wiley initially invented the SAR to enhance the resolution of side-looking radars by utilizing the Doppler spread of the signal. In the realm of remote sensing, numerous studies have been devoted to SAR image technologies for oceanography and oceanic engineering since 1955. SAR images convey insightful information on meteorological and

environmental factors, such as sea ice structures, currents, swells, gravity waves, wind speed, and direction. Due to the regular monitoring, SAR imagery is extensively employed to discern marine vessels and their distinct wave patterns. The radar footprint of the wake pattern has more prominence than the vessel's signature in SAR images, leading to more reliable detection and facilitating the extraction of the vessel's position and motion information (Chen, Chen, and Yang 2008; J. Li et al. 2021). Ship wakes appear in SAR images as long turbulent trails, V-shaped divergent wakes, and Kelvin wakes with transverse waves. The principal concern of our work is how SAR images reveal submarine manifestations. The primary wake patterns of the moving submerged vessels include Bernoulli hump, turbulent, internal, and Kelvin wakes. The movement of propeller is the primary cause of turbulent wakes. As per the literature (Xue et al. 2020), the turbulent wake is no longer visible when the submarine is fully immersed. Further, modern submarines are equipped with pump-jets to enhance stealth capabilities. Then, Kelvin wake becomes internal wake if the submarine operates below 100 m (Xue et al. 2020). However, submarines produce perceivable traces on the sea surface only when their operating depth is less than 40 m (Arivazhagan et al. 2024; Sudharsun et al. 2022). Based on the research reviews, this study models and investigates the Kelvin wake and Bernoulli hump characteristics of submarines up to a depth of 30 m.

Cutting-edge deep learning (DL) has revolutionized SAR image-based oceanographic applications like shoreline detection (Modava, Akbarizadeh, and Soroosh 2019), oil spill identification (Ghara, Shokouhi, and Akbarizadeh 2022), ship target recognition (J. Zhao et al. 2019; S. Zhao et al. 2022), ship classification (Rizaev and Achim 2022; Sharifzadeh, Akbarizadeh, and Seifi Kaviani 2019), and temporal change monitoring (Samadi, Akbarizadeh, and Kaabi 2019). A variety of machine vision models have emerged for despeckling SAR images (Vitale et al. 2025; Xu, Qi, et al. 2024). Moreover, DL-powered SAR-optical image fusion techniques have been developed for efficient detection of ship targets (Z. Zhang et al. 2024). However, DL-based wake identification in SAR imagery remains in its infancy, primarily because of the restricted access to SAR images featuring wakes. Earlier investigations exploited simulated (Rizaev and Achim 2022; J. Wang et al. 2023), actual (Del Prete, Graziano, and Renga 2021; Ding et al. 2023; Xu and Wang 2024), and a combination of real-time and modelled (L. Wang, Zhang, and Wang 2022) SAR images for ship wake detection. Of them, only the ship wake dataset released by (Xu and Wang 2024) is openly available. Anyhow, this study concentrates on the wake patterns of submerged vessels. To our knowledge, there is no dedicated dataset for SAR images of submarine wakes. Therefore, modelling them with real-time SAR image properties is crucial for generating an extensive dataset of submarine wake patterns.

The generation of geometric characteristics of ocean waves with surface wakes caused by submerged vessels is an essential prerequisite for simulating intended SAR images. Ocean dynamics can be modelled by processing sea wave spectra that capture the angular distribution and wavelength range of marine waves. Oceanographers typically utilize the WAVEWATCH – III (henceforth WW3) tool to predict the dynamics of ocean waves. To generate wave number spectra, it resolves the spectral action density equation with customized source terms (ST), incorporating factors like wind, currents, and bottom bathymetry. The effectiveness of the WW3 model is examined through several ST packages, concluding that ST4 physics yields superior performance (Amrutha et al. 2016; Mentaschi et al. 2015; Umesh and Behera 2020). Furthermore, empirically modelled

omnidirectional spectra are engaged to simulate gravity and capillary wave spectra. The Elfouhaily spectrum (Elfouhaily et al. 1997) is the most extensively employed theoretical model for radar backscattering. Then, Computational Fluid Dynamics (CFD) technology supports the mathematical modelling of sea vessel displacement. The CFD tool models the Kelvin wake (Deng, Zhang, and Wang 2019; Jia et al. 2024; Liu and Jin 2017) and Bernoulli hump (Sudharsun et al. 2022) features of submarines. However, CFD simulation is computationally intensive and requires a high-performance system. To this end, Xue et al. (2020) established potential flow theory-based submarine wake simulation analogous to CFD. Arivazhagan et al. (2024) have applied both CFD and potential flow techniques for modelling the Bernoulli hump and Kelvin wake patterns of submarines, subsequently comparing both the models.

The next pivotal step in SAR imaging involves obtaining the backscattering response of the radar signal. The radar system receives reflected signals along with timing and direction information, and manipulates the backscattered data to produce SAR images. Bragg and non-Bragg scatterings are predominant phenomena in radar echo response, occurring at moderate and steep incidence angles, respectively. Physical and geometrical optics methods can simulate specular reflection, while Bragg scattering requires perturbation theory and composite surface models. Earlier studies have extensively exploited two-scale model (TSM) (Henderson and Lewis, 1998; Valenzuela 1978; X. Ye et al. 2020) and its improved versions (Arnold-Bos, Khenchaf, and Martin 2007; D. Li et al. 2019; J. Ye et al. 2022) to simulate both Bragg and non-Bragg scattering effects of ocean waves.

Modulation theories in image-level and echo-signal-based image formation are two significant types of conventional SAR imaging algorithms. The familiar echo-signal-based imaging algorithms are Range-Doppler (Smith 1991), chirp scaling (Raney et al. 2002), omega – K (Cumming, Neo, and Wong 2003), polar format (Rigling and Moses 2004), and sparse-based compressed sensing (CS) techniques. The image-level modulation theories comprise velocity bunching (VB) (W. R. Alpers and Bruening 1986; Hasselmann et al. 1985), Lyzenga (1986, 1988), surface fragmentation (Harger 1986), and a combination of VB and surface fragmentation models (Kasilingam and Shemdin 1988). The target-focused CS techniques, such as iterative shrinkage-thresholding (IST), Fast IST, and alternating direction method of multipliers, can reliably model the SAR images of sparse scenes. The DL models in SAR imaging exclusively employ CS-based algorithms through deep unfolding network (DUN), including content-aware shrinkage dynamic DUN (Yonel, Mason, and Yazıcı 2017), sparse IST-Net (H. Zhang et al. 2022), sparse IST-Net plus (H. Zhang et al. 2023), end-to-end model (S. Zhao et al. 2021), and marine DUN (Y. Zhao et al. 2024). The SAR imaging of ship targets is the primary focus of end-to-end model and marine DUN. Nevertheless, the spatial unsparsity of wake patterns renders CS-based algorithms unreliable for SAR imaging of wake features. Accordingly, there is no prior research on DL-based SAR imaging models for wake patterns.

The SAR images of wake signatures are prevalently modelled using the VB model (Deng, Zhang, and Wang 2019; Rizaev et al. 2022; Kamirul et al. 2024; L. Wang, Zhang, and Wang 2020; L. Wang, Zhang, and Wang 2022; Zilman, Zapolski, and Marom 2014), and several research works have exploited the Range-Doppler algorithm (J. Wang et al. 2023; Jia et al. 2024; S. Wu et al. 2023; Q. Li et al. 2022). Xu, Qi, et al. (2024) leverage the omega-K algorithm to develop the turbulent wake SAR image simulator. However, these studies primarily simulate single-look SAR images and fail to examine the multi-look images.

Multi-look processing mitigates speckle effect and enhances the visual clarity, similar to spatial smoothing. Additionally, the SAR images in these investigations have been modelled without considering precise sea wave spectra in the intended observational region. Our research work purports to design a SAR image simulator capable of creating both single- and multi-look SAR images of submarine wakes, considering real-time oceanic conditions and all possible radar parameters. To fulfill this objective, the proposed research offers the following key contributions.

- (1) Ocean surfaces are modelled using linear wave theory, utilizing WW3 swell and Elfouhaily wind spectra in the Indian Ocean and Mediterranean Sea regions. To emphasize the necessity of realistic sea spectra modelling, this work leverages the WW3 tool to simulate spectra in the selected region. Then, the simulated sea waves are validated through real-time BUOY and European Centre for Medium-Range Weather Forecasts (ECMWF) data.
- (2) A novel revamped velocity bunching modulation (RVBM) mechanism is launched to model both single- and multi-look SAR images by incorporating Kaiser-Bessel function with sub-image averaging. Here, the Kaiser-Bessel weighting function plays a vital role in alleviating the speckle effect in multi-look images.
- (3) The SAR imaging of submarine manifestations is simulated over all conceivable radar scanning parameters, such as moving platform, resolution of the SAR mechanism, frequency, polarization, and incident angle of the electromagnetic signal.
- (4) To reveal the reliability of the proposed SAR imaging framework, simulated images are compared against Sentinel-1 SAR images using various qualitative and quantitative measures. Further, the performance of the proposed SAR imaging algorithm has been compared with that of existing algorithms.
- (5) Finally, the graphical user interface (GUI) is devised to assist researchers who intend to investigate the SAR imaging response of submarine wakes under various sensing parameters. This will facilitate the advancement of ground-breaking SAR imaging missions.

The remainder of the paper is structured as follows: [Section 2](#) outlines the basic principles of SAR imaging process. [Section 3](#) elaborates on the modelling methodologies of sea surfaces, submarine wakes, and SAR images. The modelling data and setup have been discussed in [Section 4](#). [Section 5](#) demonstrates the simulation and validation outcomes of the proposed method with an extensive set of experiments. Finally, [Section 6](#) conveys the conclusion of this research.

2. SAR imaging principle

Commonly, imaging radars consist of two main modules: radar hardware and signal processor. Data collection is the principal function of radar, while the signal processor is responsible for image formation. [Figure 1\(a\)](#) shows the typical SAR imaging principle of space-borne radars, whereas the functional blocks of signal processor are given in [Figure 1\(b\)](#). Most space-borne SAR relies on ground-based signal processors, whereas airborne SAR utilizes on-board signal processing. Some

advanced airborne radars combine both on-board and ground-based processing. Typically, radar hardware transmits microwave pulses towards the observation scene and collects the echo signal. After that, the signal processor stores and processes the received echo signals. The focused SAR image is produced by processing the raw signal through the following key steps: range compression, Doppler centroid and range cell migration (RCM) correction, and azimuth compression, as in Figure 1(b).

The range-compressed image can be referred as RAR image, the unfocused image is geometrically corrected one, and the azimuth-compressed image is defined as focused SAR image. Subsequently, the detector is applied to generate the squared magnitude of SAR images, as the focused SAR image is in complex (magnitude and phase) form. In the

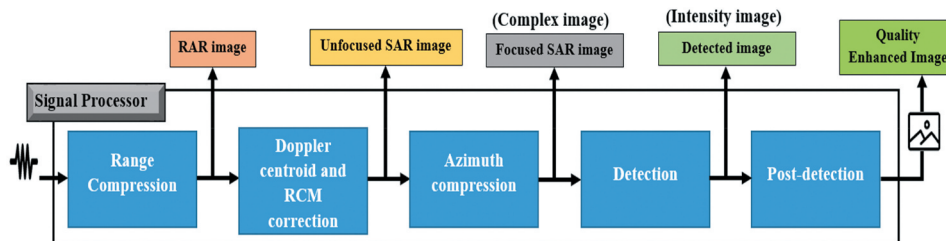
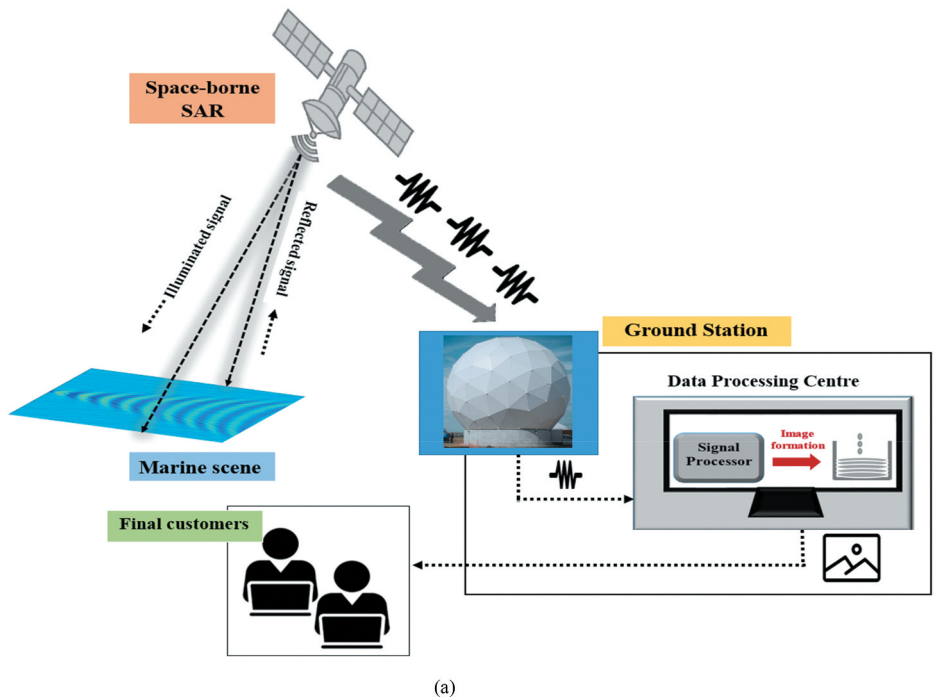


Figure 1. Representation of (a) SAR imaging principle of space-borne radars (b) functional blocks of signal processor.

end, post-detection is employed to enhance the image quality and reduce the data storage. Radiometric correction, geometric correction, and speckle filtering are familiar post-detection strategies.

In radar terms, azimuthal means the direction along the trajectory of aerospace vehicles, while the direction normal to the trajectory is called range. Range and azimuth compression are pulse compression techniques employed to attain high resolution along respective directions. Pulse compression is achieved through the matched filter by correlating transmitted and received signals. Normally, the transmitted signals are represented as chirp pulses along range plane and are intrinsically formed in azimuth path by Doppler correction in SAR imaging systems. Doppler centroid deviation and RCM are scatter barriers in SAR system, created by geometric distortion and platform motion. The issues mentioned are addressed by analysing frequency response along the flight path and applying interpolation in range direction. In real-time, all of these preceding steps are performed by signal processor to produce the final SAR image.

The echo signal-based SAR imaging techniques adhere to the aforementioned actual-time processes to create focused SAR images. Nevertheless, modulation-based imaging theory differs from traditional methodology. At first, the modulation-based technique was applied to SAR images to extract sea spectra (W. Alpers and Hasselmann 1978). As in Equation (1), the connection between sea and SAR spectra can be established by the modulation transfer mechanism (MTM), which considers the tilt and hydrodynamic transformation of sea waves. Later, the inverse of this process was acquainted in SAR image simulations (Hasselmann et al. 1985; W. Alpers 1983; W. R. Alpers and Bruening 1986), incorporating velocity bunching effect (W. Alpers and Rufenach 1979).

$$F_{sea}(K, \varphi) = (F_{SAR}(K, \varphi)) / (M(K, \varphi)) \quad (1)$$

where, $F_{sea}(K, \varphi)$ and $F_{SAR}(K, \varphi)$ are sea wave and SAR spectra, respectively, and $M(K, \varphi)$ is spectra of MTM.

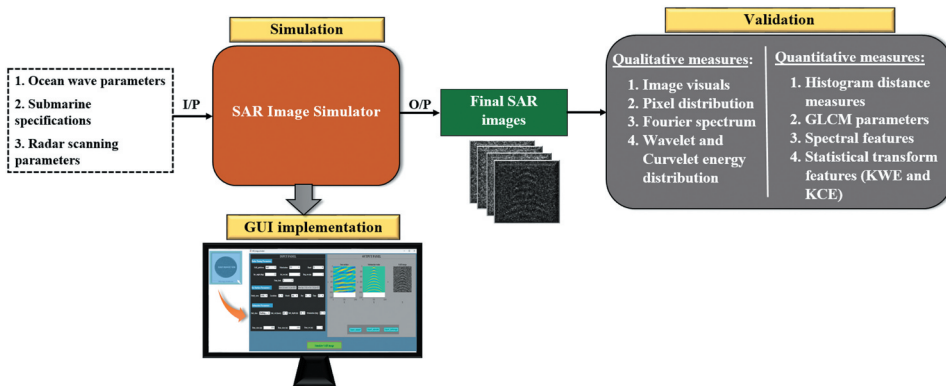
In the VB-based imaging framework, the repercussion of motion over range axis has been ignored because range perception happens at light speed. Thus, pioneers presumed that the backscattered response should already be range-focused. The image focusing on flight direction is done through dechirping, as mentioned in Equation (2). This equation has been utilized to recreate the focused SAR image in VB model, excluding speckle effect.

$$I_{C_SAR} = (G * h) \times A \quad (2)$$

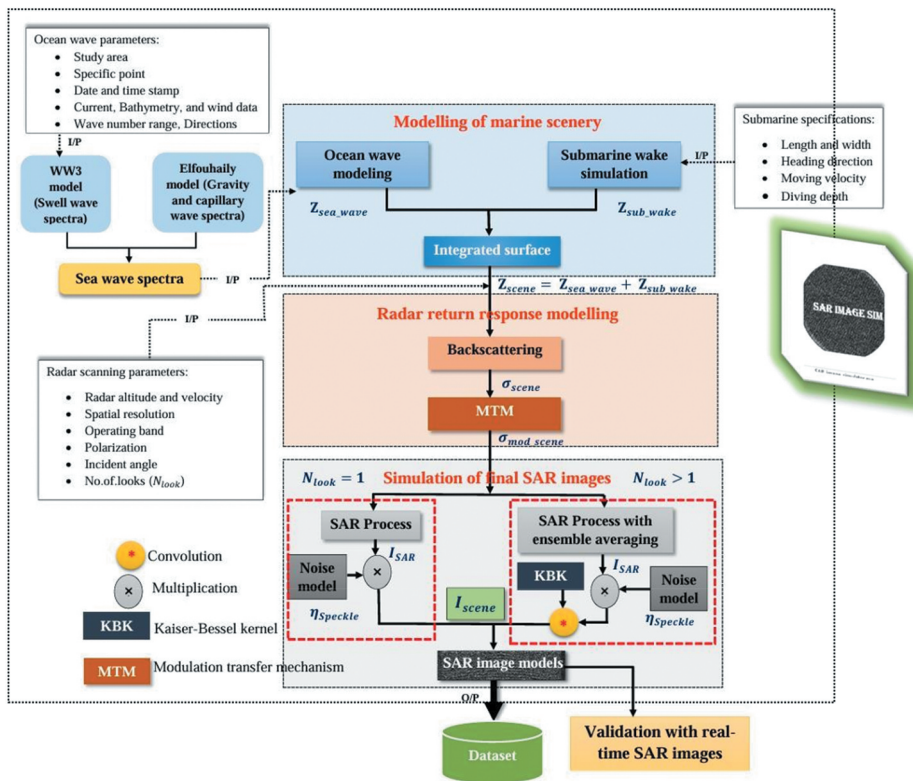
where, I_{C_SAR} denotes complex SAR image, A is scattering signal amplitude, h is transfer function of matched filter, and G is Gaussian antenna pattern. These functions are scrupulously specified in W. Alpers and Rufenach (1979).

3. Modelling methods

Figure 2(a) illustrates overall framework of the proposed work. Initially, SAR image simulator generates SAR images of submarine manifestations by utilizing oceanic, submarine, and radar scanning parameters. Then, simulated SAR images undergo evaluation using real-time images. Finally, the GUI has been implemented to enable



(a)



(b)

Figure 2. (a) Overall framework of the proposed work (b) proposed SAR image simulator system.

the efficient examination of the simulated SAR images. The present work utilizes the MATLAB 'app designer' tool to build the GUI model. The functional block diagram of the proposed SAR image simulator is presented in Figure 2(b). The design of SAR image simulator has three distinct stages: simulating radar viewpoints, modelling the radar return response, and creating the final SAR images. At first, the ocean surface

scene (Z_{scene}) is created by integrating the modelled sea surface (Z_{sea_wave}) and submarine wake (Z_{sub_wake}). Then, the backscattered response (σ_{scene}) of the view-points is simulated using the specified electromagnetic wave parameters. The modulated radar returns (σ_{mod_scene}) include tilt, hydrodynamic, and bunching effects. Further, modulated scene undergoes azimuthal processing to produce the SAR image (I_{SAR}) according to the proposed RVBM algorithm. In order to get the final SAR image (I_{scene}), processed image (I_{SAR}) is multiplied by the speckle noise ($\eta_{speckle}$) in single-look processing. For multi-look processing, the noise-inserted SAR image is convolved with the Kaiser kernel to produce a smoothed SAR image (I_{scene}).

3.1. Stage 1: radar view-point simulation

In the present work, the radar field of view is deemed to be sea waves interspersed with subsurface vessel wakes. To accomplish this task, one needs to model ocean surface waves with the disturbance caused by the submarine movements. This stage entails modelling of sea wave dynamics, simulation of submarine wakes, and its integration.

3.1.1. Modelling of sea wave dynamics

Regionally generated wind waves and distant-travelling swell waves contribute to the dynamism of ocean waves. The topography of the sea surface is prevalently modelled using Airy theory (Holthuijsen 2010). Equation (3) generates the elevation of the sea surface model (Z_{sea_wave}).

$$Z_{sea_wave} = \sum_{m=1}^{len(K)} \sum_{n=1}^{len(\phi)} A_{mn} \cos(xK\cos\phi + yK\sin\phi - (\omega_m t) + (\phi_{mn})) \quad (3)$$

where, x and y define the ocean surface coordinates, K represents magnitude of spatial frequencies (rad/m), ϕ is distinct directions of waves (degrees), ϕ indicates uniformly distributed phase function, ω is angular frequencies (rad/s), and t denotes the time frame. In the following analysis, t is assumed to be 1. Equation (4) computes angular frequency, which quantifies phase variation of sea waves over time.

$$\omega = (gK)^{0.5} \quad (4)$$

where, g is acceleration constant ($g = 9.8ms^{-2}$).

Equation (5) symbolizes the amplitude of sea waves, which significantly controls their patterns.

$$A_{mn} = \sqrt{2F(K_m, \phi_n) \nabla K_m \nabla \phi_n} \quad (5)$$

where, K_m and ϕ_n are stride sizes of spatial frequencies and wave directions. In our work, the 2D – sea wave spectra ($F(K_m, \phi_n)$) are formed by combining swell ($F_{swell}(K_m, \phi_n)$) and wind ($F_{wind}(K_m, \phi_n)$) wave spectra, as in Equation (6). The ocean wave spectrum at the specified area is modelled through WW3 platform, and the local wind waves are formed using various gravity – capillary wave spectrum.

$$F(K_m, \phi_n) = F_{swell}(K_m, \phi_n) + F_{wind}(K_m, \phi_n) \quad (6)$$

WW3 model: To deliver the wave spectra, WW3 solves the spectral energy balance in Equation (7).

$$\frac{\partial F_a}{\partial t} + \nabla \cdot \dot{X}N + \frac{\partial}{\partial K} \dot{K}N + \frac{\partial}{\partial \phi} \dot{\phi}N = \frac{ST}{\sigma_i} \quad (7)$$

where, F_a represents the wave action spectrum, t denotes time, σ_i is the intrinsic frequency, K is the wave number, θ is the wave directions, ∇ indicates spatial gradient along x -direction, X is addition of group velocity and current velocity, the over-dot represents the rate of change, and ST refers to source terms. The source term regulates the physical processes that influence the progress of ocean waves. In this work, swell dissipation is enabled through ST4 package (Ardhuin et al. 2010) to generate swell wave spectra.

Wind-wave models: The WW3 model is typically designed for large-scale waves. Thus, a predefined wind wave spectrum is affixed with the simulated swell spectrum to observe the roughness in the stated area. This study examines ocean surface coarseness using Elfouhaily spectrum. The spectrum and the necessary parameters are derived from the original article (Elfouhaily et al. 1997).

3.1.2. Simulation of submarine wakes

This study adopts the SPPIC technique (Arivazhagan et al. 2024) to create submarine wakes, which simulate them based on Equation (8).

$$Z_{sub_wake}(x, y) = \frac{v}{g} \begin{cases} \left. \frac{\partial \Phi_{sub_wake}}{\partial x} \right|_{z=0} & ; \theta_{dir} = 0^\circ, 180^\circ \\ \left. \frac{\partial \Phi_{sub_wake}}{\partial y} \right|_{z=0} & ; \theta_{dir} = 90^\circ, 270^\circ \\ \left(\left. \frac{\partial \Phi_{sub_wake}}{\partial x} + \frac{\partial \Phi_{sub_wake}}{\partial y} \right) \right|_{z=0} & ; elsewhere \end{cases} \quad (8)$$

where, Z_{sub_wake} denotes submarine wake elevation, v is moving speed of submerged vessel (m/s), θ_{dir} represents the moving direction of the submarine according to the radar view, and Φ_{sub_wake} indicates velocity potential, which is estimated from the literature (Arivazhagan et al. 2024).

Then, the final radar scene is created by integrating sea surface and submarine wake elevation, as stated in Equation (9).

$$Z_{scene} = Z_{sea} + Z_{sub_wake} \quad (9)$$

3.2. Stage 2: modelling of radar return response

By incorporating a weighted sum of GO and composite Bragg theory (Arnold-Bos, Khenchaf, and Martin 2007), the TSM model accurately reproduces the backscattering response, as indicated in Equation (10).

$$\sigma_{scene}(x, y) = (1 - w) \left(\frac{|R(0)|^2}{s^2} \sec^4 \theta_l e^{\left(\frac{-\tan^2 \theta_l}{s^2} \right)} \right) + w \left(16\pi k_e^4 \cos^4(\theta_l) |a_{pq}|^2 F(k_{Bx}, k_{By}) \right) \quad (10)$$

where, $|R(0)|$ is Fresnel reflection coefficient, θ_l is local incident angle, s^2 denotes variance of the surface slope, k_e is wave number of EM waves, and $F(k_{Bx}, k_{By})$ represents sea wave spectrum at Bragg wave numbers.

The composite Bragg theory models the Bragg scattering phenomena of ocean surfaces, whereas the GO technique deals with specular reflection. According to composite Bragg theory, sea surfaces are treated as a collection of rough patches consisting of small-scale waves that are tilted by large waves (X. Ye et al. 2020). The composite Bragg theory accounts for the tilt effect, whereas Bragg theory excludes it. The scattering function (a_{pq}) reflects the influence of the tilt effect. The subscripts p and q in a_{pq} denote polarization mode, either V or H. a_{VV} , a_{HH} , and a_{VH} values are obtained from Valenzuela (1978). The weighting function (w) mitigates the sharp shift between these two backscattering models, and it can be estimated through Equation (11). The remaining attributes are adopted from Arnold-Bos, Khenchaf, and Martin (2007) and J. Ye et al. (2022).

$$w = \begin{cases} 10 \left(-\left(\frac{\theta_l}{20\pi} \right)^8 \right); p = q \\ 10 \left(-\left(\frac{\theta_l}{20\pi} \right)^{1.5} \right); p \neq q \end{cases} \quad (11)$$

Then, the MTM incorporates the sea wave fluctuation, as depicted in Equation (12). Here, MTM encompasses tilt ($M_t(K)$), hydrodynamic ($M_h(K)$), and bunching effects ($M_{vb}(K)$) that are taken from W. R. Alpers, Ross, and Rufenach (1981).

$$\sigma_{mod_scene}(x, y) = \sigma_{scene}(x, y) \left(1 + \int^{M(K)F[Z_{sea_wave}]e^{ik_y}} dk \right) \quad (12)$$

where, $F[Z_{sea_wave}]$ denotes Fourier response of sea surface, $M(K)$ is modulation function and is given in Equation (13).

$$M(K) = M_t(K) + M_h(K) + M_{vb}(K) \quad (13)$$

3.3. Stage 3: simulation of final SAR images

This study offers a revamped velocity bunching modulation mechanism to generate both single- and multi-look SAR images. Equation (14) creates speckle-free single-look SAR image intensity, which is obtained from Equation (2). Multi-look processing was introduced by Raney, 1980 to enhance the image quality. The SAR processor divides the entire aperture length into sub-apertures during multi-look processing over a single acquisition. Thus, there is a discrepancy between the SAR antenna observation time and the processor integration time. According to Equations (15) and (16), multi-look processing reduces processor integration time and azimuth resolution. Rufenach and Alpers (2003) discuss the implications of orbital motion on multi-look processing. However, prior researchers forgot to incorporate the averaging of sub-images with look extraction filter in VB model. The RVBM approach outlined in Algorithm 1 addresses this case by utilizing the Kaiser-Bessel function (Henderson and Lewis, 1998) specified in Equation (17). Here, the speckle effect is modelled with an exponential distribution across all scenarios.

$$I_{\text{inten_SAR}}(x_i, y_i) = |I_{C_SAR}|^2 = \frac{\pi(T_{\text{int}}')^2}{2} \iint \delta(x_i - x) \frac{\sigma_{\text{mod_scene}}(x, y) r_{\text{azi}}'}{\rho_a'(x, y)} \exp \left\{ -\pi^2 \left[\frac{y_i - y - (R/V) \widetilde{U_r(x, y)}}{\rho_a'(x, y)} \right]^2 \right\} dx dy \quad (14)$$

where, R is range distance, V is moving velocity of the SAR platform, $\widetilde{U_r(x, y)}$ is mean radial velocity, $\rho_a'(x, y)$ is degraded azimuthal resolution, and $\delta(x_i - x)$ is impulse function that specifies range focusing along range direction by substituting $x = x_i$.

$$T_{\text{int}}' = T_{\text{int}}/N_{\text{look}} \quad (15)$$

$$r_{\text{azi}}' = r_{\text{azi}} N_{\text{look}} \quad (16)$$

where, T_{int}' and r_{azi}' define updated integration time and azimuth resolution concerning the number of looks (N_{look}).

$$W(n) = \frac{W_0 \left(\beta \sqrt{1 - \left(\frac{n-L/2}{L/2} \right)^2} \right)}{W_{0(\beta)}}, 0 \leq n \leq L-1 \quad (17)$$

where, W_0 denotes zeroth-order Bessel function, β is shape factor, L indicates length of the window, and n is the corresponding point.

The mean radial velocity and acceleration can be calculated using Equations (18) and (19).

$$\widetilde{U_r(x, y)} = \text{Re}(\text{IFFT}(\text{FFT}(U_r(x, y)).ff)) \quad (18)$$

$$\widetilde{A_r(x, y)} = \text{Re}(\text{IFFT}(\text{FFT}(A_r(x, y)).ff)) \quad (19)$$

where, ff is filtering factor, U_r and A_r denote radial velocity and acceleration of the marine scene, and are computed as in Rizaev et al. (2022).

4. Data and WW3 model setup

4.1. Study area

The SAR imaging models are simulated and validated in two different areas. Study area 1 involves East Coast of India (ECI), while the second area is Gulf of Genoa (GOG), Italy.

4.1.1. Study area 1

Initially, this study chooses the coastal areas around Indian Ocean region to observe and analyse the SAR images of the ocean surface in India. The WW3 spectra are modelled in the Indian Ocean region between 1 September 2017, and 30 October 2017, since the real-time Sentinel –1 swell spectra (OCN product) and corresponding SAR images (SLC product) are available within that time frame. This will be beneficial for model validation. As seen in Figure 3(a), two grids are used to model the ocean wave spectra at ECI: the Indian Ocean is the outer grid

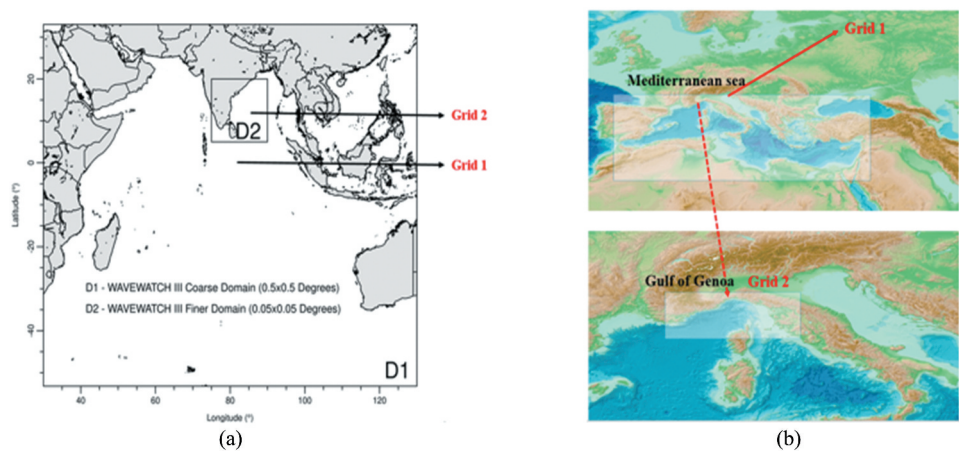


Figure 3. Grids of (a) study area 1 (b) study area 2.

and the Bay of Bengal is the inner grid. The latitude and longitude ranges of grid 1 are -72° S to 35° N and 30° W – 130° E, whereas grid 2's ranges are 5° S to 20° N and 75° W to 90° E, respectively. The model outputs are taken from ten different locations, and the points are mentioned in bottom right corner of Figure 4. The points are selected based on the location of the BUOY data and Sentinel –1 SAR data.

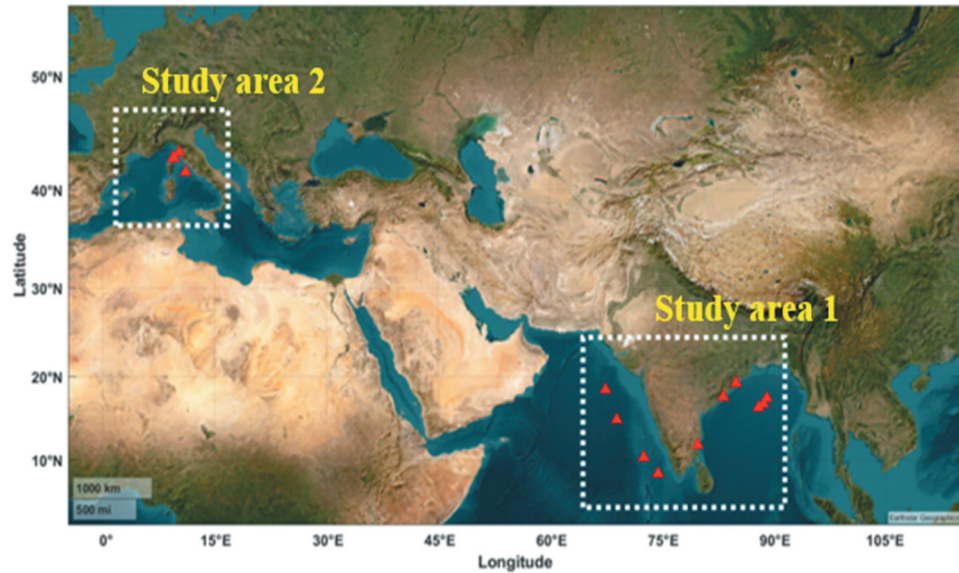


Figure 4. Data point locations of both study areas.

4.1.2. Study area 2

Algorithm 1 Revamped Velocity Bunching Modulation Algorithm

Input: Modulated backscattered response (σ_{mod_scene}),
Radar scanning parameters: Platform height (H), velocity (V), incident angle (θ_g), number of looks (N_{look}), range (r_{range}) and azimuth (r_{azi}) resolution,
Mean radial velocity and acceleration ($U_r(\widetilde{x}, y)$, $A_r(\widetilde{x}, y)$)

Output: Intensity of the SAR image I_{scene}

```

1: function SAR_imaging
2:   Initialize scene coherence time  $\tau_c$  and processed SAR image  $I_{SAR}$ 
      
$$\tau_c = \begin{cases} 0.0345; & \text{if } \lambda = 0.031 \\ 0.063; & \text{else if } \lambda = 0.057 \\ 0.261; & \text{else if } \lambda = 0.261 \end{cases}$$

      
$$[r, c] = \text{size}(\sigma_{mod\_scene})$$

      
$$I_{SAR} = \text{zeros}(\text{round}(r/r_{range}), \text{round}(c/r_{azi}))$$

3:   Calculate slant range ( $R_s$ ), ground range ( $R_g$ ), and integration time ( $T_{int}$ ) values
      
$$R_s = \frac{H}{\cos\theta_g}$$

      
$$R_g = R_s \sin\theta_g$$

      
$$R = \begin{cases} R_s; & N_{look} = 1 \\ R_g; & N_{look} > 1 \end{cases}$$

      
$$T_{int} = \frac{AR}{2Vr_{azi}}$$

4:   Compute degraded azimuth function
      
$$\rho_a'(x, y) = r_{azi}' \left[ 1 + \left( \frac{(T_{int}')^4 \pi^2}{\lambda^2} A_r(\widetilde{x}, y)^2 \right) + \left( \frac{(T_{int}')^2}{\tau_c^2} \right) \right]^{0.5}$$

5:   Update backscattered response and degraded azimuthal function
      
$$\sigma_{mod\_scene} = \sigma_{mod\_scene}(1:r_{range}:end, 1:r_{azi}:end)$$

      
$$\rho_a' = \rho_a'(1:r_{range}:end, 1:r_{azi}:end)$$

6:   Estimate exponential noise distribution
      
$$\eta_{speckle} = \text{exprnd}(1, [r, c])$$

7:   for  $i = 1:1:N_{look}$ 
      temp_img =  $I_{inten\_SAR}$ ; (Calculate  $I_{inten\_SAR}$  using equation (14))
      
$$I_{SAR} = I_{SAR} + I_{inten\_SAR};$$

8:   End
9:   Find intensity of final SAR image  $I_{scene}$ 
10:  if  $N_{look} > 1$ 
11:    Calculate temporary image
      
$$I_{temp} = I_{SAR} \cdot \eta_{speckle}$$

12:    Determine Kaiser-Bessel kernel
      Calculate  $W$  using equation (17)
      
$$KBK = WW'$$

      
$$I_{scene} = I_{temp} * KBK$$

13:  Else
      
$$I_{scene} = I_{SAR} \cdot \eta_{speckle}$$

14:  End
15:  return  $I_{scene}$ 
16: end function

```

Although the Indian Ocean region has the highest volume of ship commutes, we couldn't get Automatic Identification System (AIS) information regarding sea vessels in that area. Hence, the Gulf of Genoa in Italy is chosen as the second focal location to verify the simulated SAR images containing vessel wakes since AIS data for ships in this region are available in the literature (Graziano and Renga 2021). This site encompasses two grids: Mediterranean Sea and Gulf of Genoa, as depicted in Figure 3(b). Latitudes 29° S to 44° N and longitudes −5° W to 36° E are the boundaries of the Mediterranean Sea. Second, the Gulf of Genoa covers the latitudes 42° S to 44° N and longitudes 6.5° W to 10.5° E. Further,

the pertinent Sentinel –1 product (S1A_IW_GRDH_1SDV_20200706T171436_20200706T171501_033337_03DCC6_1122) is recorded on 6 July 2020. Thus, WW3 spectra are generated for the period from 1 July 2020 to 6 July 2020. The spectral outputs are collected from ten points, as indicated in [Figure 4](#) (left side). Here, the spots are picked according to the availability of ships with AIS data.

In this article, study area 1 is utilized to examine the swell waves in SAR images, and the points in study area 2 are exploited to verify the SAR images of sea surface embedded with wake patterns.

4.2. WW3 model setup

The WW3 model encompasses various stages, including grid generation, pre-processing, model execution, and post processing. The WW3 tool is tuned according to the inputs provided to the model, and the model outputs are obtained from the designated locations. The exact position and name of the model output points of both study areas are listed in [Table 1](#). For study area 1, the points are located in the Arabian Sea (Moored BUOY AD series), Bay of Bengal (Moored BUOY BD series), and East Coast area (BUOYPOND, BUOYVIZA, BUOYGOPA). The points SAR1W11 and SAR1W21 correspond to SAR Sentinel –1 data. Then, the study area 2 points are situated in the ship locations at GOG. Here, MEGA_EXP1 to MEGA_EXP5 stand for the five distinct places near the ship known as MEGA_EXPRESS. Then, MSC_NITYA1 and MSC_NITYA2 correspond to two locations close to the vessel MSC_NITYAB. LA_SUPERB1 and LA_SUPERB2 denote the points near the ship LA_SUPERBA. Finally, the MOBY_AKI point indicates the position of the surface vessel MOBY_AKI. A detailed explanation of these ships will be discussed in section 5.3.2.

The WW3 model setup details of each study area are given in [Table 2](#). The model utilizes the European Centre for Medium-Range Weather Forecasts (ECMWF) reanalysis version 5 (ERA5) wind data, General Bathymetric Chart of the Oceans (GEBCO) and earth topography (ETOPO2) bathymetry records, and ocean surface current analysis real-time (OSCAR) data system which provides the current information. The ECMWF ERA5 wind data has an hourly temporal resolution and a $0.25^{\circ} \times 0.25^{\circ}$ geographic resolution. For OSCAR data, the spatial and temporal granularities are $0.33^{\circ} \times 0.33^{\circ}$ and five days.

For grid generation, the WW3 model leverages 2D rectilinear nested grids. There are two grids in study areas 1 and 2, as mentioned earlier. Study area 1 has the resolution of 0.5° and 0.05° for grids 1 and 2 in both coordinates, respectively. Then, grids 1 and 2 in

Table 1. Three model point list.

S.No	Study area 1	Study area 2
1.	BUOYAD06 (+18.495, +67.450)	MEGA_EXP1 (+43.038, +9.4957)
2.	BUOYAD07 (+14.931, +68.976)	MEGA_EXP2 (+43.040, +9.491)
3.	BUOYAD10 (+10.322, +72.587)	MEGA_EXP3 (+43.043, +9.487)
4.	BUOYBD10 (+16.362, +87.990)	MEGA_EXP4 (+43.050, +9.4778)
5.	BUOYBD09 (+17.500, +89.117)	MEGA_EXP5 (+43.052, +9.474)
6.	SAR1W11 (+8.332, +74.517)	MSC_NITYA1 (+43.004, +9.5983)
7.	SAR1W21 (+16.812, +88.632)	MSC_NITYA2 (+43.005, +9.5981)
8.	BUOYPOND (+11.870, +79.840)	LA_SUPERB1 (+43.527, +10.266)
9.	BUOYVIZA (+17.630, +83.270)	LA_SUPERB2 (+43.529, +10.269)
10.	BUOYGOPA (+19.270, +84.970)	MOBY_AKI (+41.7287, +11.123)

Table 2. Three model inputs.

WWIII model inputs	Simulation parameters	
	Study area 1	Study area 2
Grid 1 resolution	$0.5^{\circ} \times 0.5^{\circ}$ (55.5 km \times 55.5 km)	$0.1^{\circ} \times 0.1^{\circ}$ (11.1 km \times 11.1 km)
Grid 2 resolution	$0.05^{\circ} \times 0.05^{\circ}$ (5.5 km \times 5.5 km)	$0.025^{\circ} \times 0.025^{\circ}$ (2.77 km \times 2.77 km)
Simulation period	September 1 - October 30, 2017	July 1 - 6, 2020
Temporal resolution	1 hr	
Spectral discretization	Frequency range: 0.0373 to 0.2 (32 bins) Direction range: 0° to 360° (24 bins)	
Model physics	ST4	
Wind	ECMWF ERA-5 (0.25° grid resolution)	
Current	OSCAR (0.33° spatial resolution and the temporal resolution is 5 days)	
Bathymetry	GEBCO and ETOPO2	

study area 2 have precision of $0.1^{\circ} \times 0.1^{\circ}$ and $0.025^{\circ} \times 0.025^{\circ}$. The bathymetry data is the major input needed to create the grid. Here, the outer grid is established using GEBCO bathymetry, while the inner grid is generated by utilizing ETOPO-2 bathymetry.

The model grids, spectrum point grids, and model forcing field (wind and current data) grids are configured in the pre-processing stage. The WW3 grid pre-processor utilizes spectral discretization with thirty-two frequencies and twenty-four directions. The frequencies follow a logarithmic distribution, starting at 0.0373 Hz and ending at 0.2 Hz. The wave directions span from 0° to 360° , with a resolution of 15° .

During WW3 run, equations calculate the evolution of wave energy across the simulated ocean surface based on wind-wave generation, nonlinear interactions, and dissipation processes. The Courant- Friedrichs-Lewy (CFL) time step is applied for the global grid. CFL defines the numerical stability in the simulations. The model updates the wave spectrum at discrete time intervals.

The output of the model is a network common data form (netCDF or.nc) file that includes the wave spectrum, significant wave height, latitude, longitude, wind speed, and wind direction of a specific location. The simulation period for study area 1 is two months with a time step of one hour. Thus, the dimensions of the output data for September and October are 10×720 (two netCDF files). The model is executed over six days to analyse study area 2, using a time step of one hour. The output data in study area 2 has a size of 10×144 (single.nc file).

5. Simulation results and discussion

The entire research work is performed using WW3 tool (version 6.07) and MATLAB software (2024b) in an Intel(R) i7 (8 core) graphics system with 2.9 GHz speed of clock and 32 GB of physical memory. The WW3 framework is written in FORTRAN 90 and is enforced in the Ubuntu (20.04 LTS) operating system using Linux commands. Then, the final SAR image simulation is executed, verified, and explored in MATLAB.

5.1. WW3 modelling outcomes and validation

5.1.1. Ocean wave modelling

Ocean wave modelling is carried out in the MATLAB platform. To perform this task, WW3 swell wave spectra are extracted from netCDF files through 'ncread' command. Here,

three netCDF files have been exported from WW3 for the two study areas. The significant wave height (SWH) distributions of both the study areas are depicted in Figure 5. Figures 5(a) and 5(b) denote the SWH spread of study area 1 on 15 September 2017, at 12:00 am for grid 1 and grid 2, respectively. The distribution of significant wave heights on the modelled sea surface of grids 1 and 2 in study area 2 at 5:00 pm on 6 July 2020 is seen in Figures 5(c) and 5(d). The depictions ratify that WW3 model can simulate sea wave spectra in lower sea and higher sea conditions.

Figure 6 displays the spectral outcomes of two locations in both the study areas, with and without wind wave spectra. Figures 6(a) and 6(c) illustrate swell wave spectra captured at BUOYPOND and MEGA_EXP1 regions on the aforementioned timestamps. In contrast, Figures 6(b) and 6(d) provide the related swell distribution with wind spectra. Wind speed and direction values are extracted from WW3 output files to create wind spectrum. In this instance, Elfouhaily wind wave spectrum is modelled with 120 logarithmically divided wave numbers of 0.005 to 5 rad/m. Then, 72 spreading directions are selected from 0° to 360°, with an incremental stride of 5°. Finally, combined spectra are developed through the ensuing steps: (i) frequency-to-wave number conversion and interpolation of swell spectra, (ii) assimilation of swell and wind wave spectra.

Next, sea surface is simulated with the domain size of 1 km × 1 km. The associated sea wave models of the spectra presented in Figure 6 are given in Figure 7. Figures 7(b) and 7(d) depict the impact of wind waves on the ocean surface. In Figure 7(d), wind waves

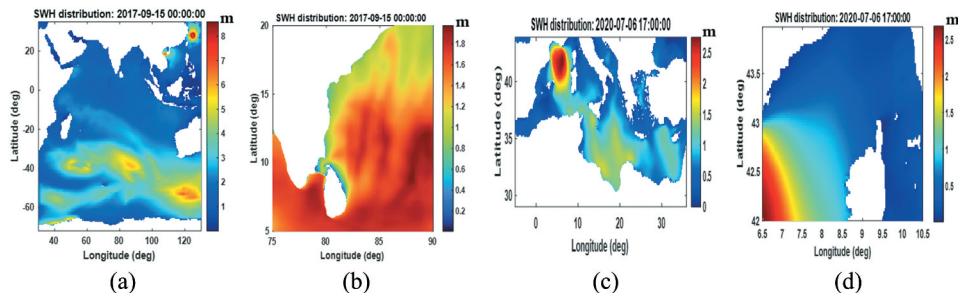


Figure 5. Significant wave height profile of (a) grid 1 and (b) grid 2 in study area 1 (c) grid 1 and (d) grid 2 in study area 2.

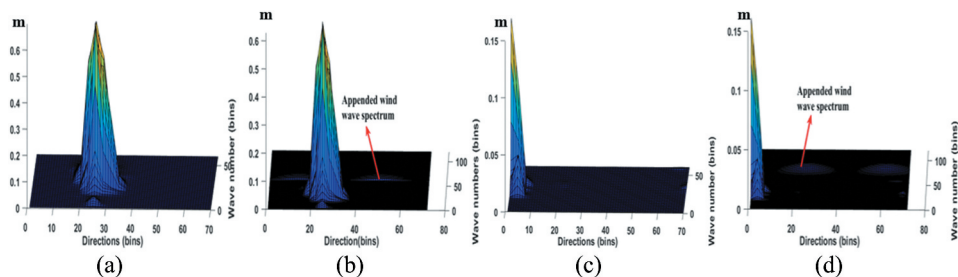


Figure 6. 2D wave spectra (a, b) at BUOYPOND location without/with wind profile (c, d) at MEGA_EXP1 region without/with wind spectrum.

overshadow the swell, compared to Figure 7 (b). This implies that the MEGA_EXP1 location experiences a lower sea state on the specified timestamp.

5.1.2. WW3 model validation

The modelled spectra of study area 1 are evaluated through BUOY data, and Sentinel-1 sea wave spectra. Further, study area 2 spectra are validated only through ECMWF data since there is no accessible BUOY. At first, the WW3 model has been verified by comparing the SWH values of the modelled sea surface with actual BUOY data. Three wave rider BUOY sites (Gopalpur, Visakhapatnam, and Pondicherry) near the grid-2 region are elected to accomplish this task. The SWH measures of BUOY stations are collected from the Indian National Centre for Ocean Information Services (INCOIS) website. The SWH values at BUOYPOND, BUOYVIZA, and BUOYGOPA points are assessed against respective BUOY data, as in Figure 8. All of the items are identified at 12:00 am between 10 September 2017 and 25 October 2017, with a five-day interval. This bar chart indicates that modelled SWH values converge with the BUOY measurements, with the maximum noted error in SWH being 0.2 m. Additionally, the familiar statistical measures like correlation coefficient (R), bias (B), root mean square error (RMSE), and scatter index (SI) values (H. Wang et al. 2021, Soran, Amarouche, and Akpinar 2022) are calculated at those three sites with 1188 samples and are tabulated in Table 3. Table 3 confirms that the actual BUOY and modelled data have a stronger association, as indicated by lower RMSE, SI, and optimal R values.

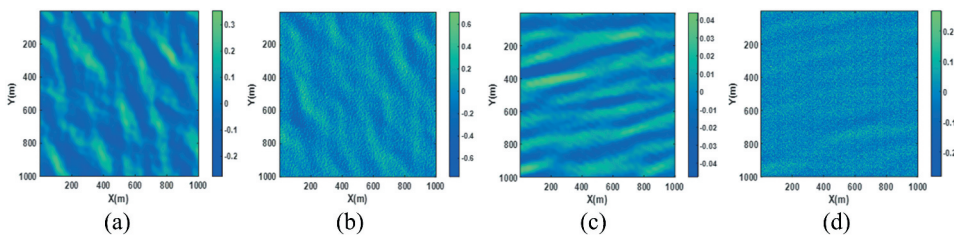


Figure 7. (a–d) modelled ocean surfaces corresponding to the spectra in Figure 6 (a–d).

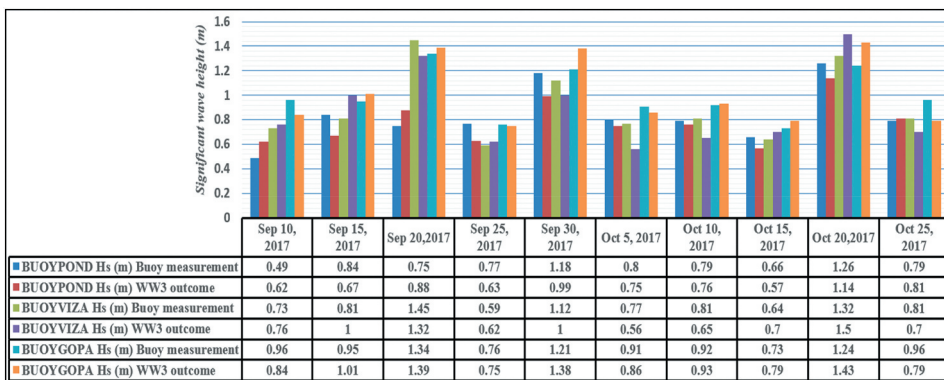


Figure 8. Significant wave height comparison between WW3 results and BUOY data.

Table 3. WW3 model statistical deviation in SWH measurement.

	BUOYPOND	BUOYVIZA	BUOYGOPA
No. of. Samples	1188	1188	1188
Correlation coefficient	0.84	0.88	0.82
Bias (m)	0.031	−0.018	−0.075
RMSE (m)	0.13	0.115	0.143
Scatter index (%)	14.19	11.39	16.91

Moreover, the direct spectrum comparison can be performed through sentinel –1 level 2 (OCN) data. Generally, Sentinel-1 level 2 products offer.nc files that contain wind speed, direction, latitude, longitude, and spectrum information. The available swell spectrum has sixty logarithmically distributed wave numbers (0.0056 – 0.2 rad/m), and seventy-two wave directions (0° to 355°). In our case, two different level 2 products (S1A_WV_OCN__2SSV_20170905T005739_20170905T011758_018233_01EA70_D85E, S1A_WV_OCN__2SSV_20171029T000558_20171029T002843_019020_02028A_2BE2) are downloaded from the Copernicus website at SAR1W11 and SAR1W21 spots on 5 September 2017 and 29 October 2017. Figure 9 displays a comparison of the WW3 model and Sentinel- 1 spectra. The Sentinel –1 and WW3 model spectra at SAR1W11 position are given in Figures 9(a,b), whilst Figures 9(c,d) denote the spectra at SAR1W21 point. The consistency in these spectra rigorously assures the reliability of WW3 swell spectra.

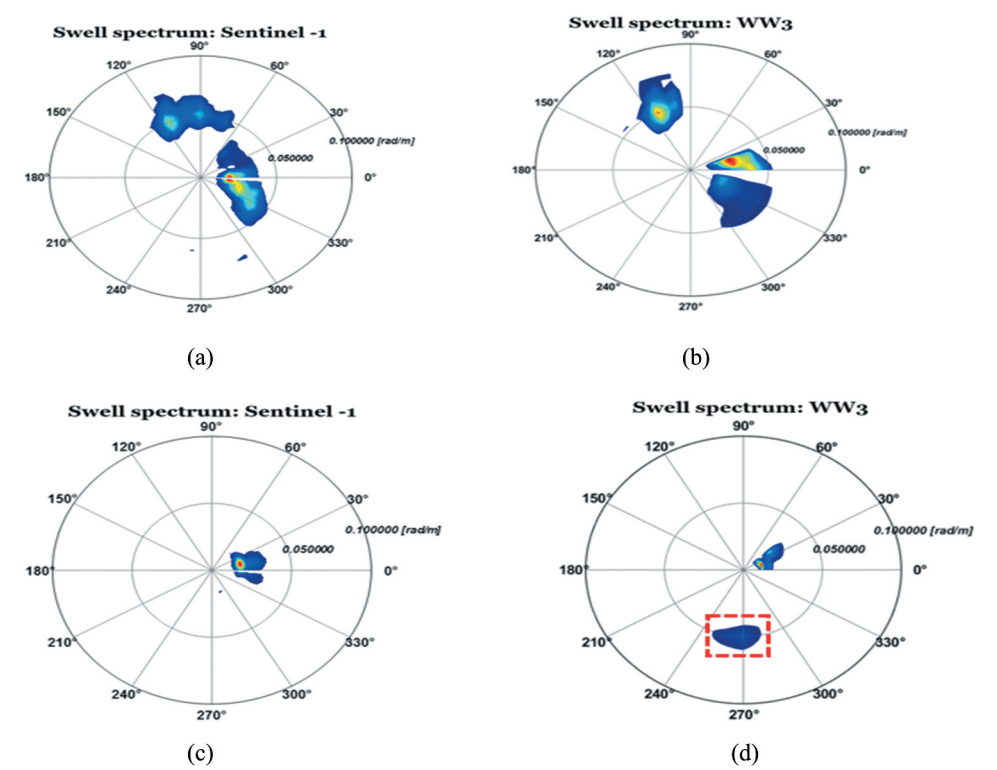


Figure 9. Swell wave spectra of sentinel- 1 and WW3 model (a, b) at SAR1W11 (c, d) at SAR1W21.

For study area 2, the SWH data are examined with the ECMWF data in the climate data store. Figure 10 shows the comparative results of SWH values at the MEGA_EXP1, MSC_NITYA1, and MOBY_AKI locations dated 6 July 2020. Our study evaluates R, B, RMSE, and SI based on 240 data points collected on 6 July 2020, yielding the values of 0.82, -0.025 m, 0.13 m, and 16.55%, respectively. The values imply the good performance of the WW3 model.

5.2. Performance of the proposed SAR imaging system

The effectiveness of the proposed SAR imaging system can be elucidated through ten potential test cases. In this instance, the sea surfaces are derived using WW3 spectra and Elfouhaily wind wave spectra. The WW3 swell spectrum in the GOG, MEGA_EXP1 location on 6 July 2020, at 5:00 pm is taken into account for simulations, except for test case 5. Further, the Sindhughosh submarine model is considered for wake generation. In the following cases, scene size of the ocean surface is defined as $1\text{ km} \times 1\text{ km}$ with 1 m resolution. The tuning parameters for each test case are given in Table 4.

Test case 1: SAR images at different imaging platforms

This paper exhibits the SAR imaging outcomes of four distinct operating platforms. The altitude and moving velocities of SAR platforms are given in second column of Table 5. Figure 11 portrays the influence of imaging platforms in SAR image simulation. The SAR images in Figure 11 show that as the platform's altitude increases, the visibility of the wake structure decreases. Further, the stability of the platform impacts image quality during image acquisition. That is, the SAR image precision will degrade as the platform's velocity increases.

Test case 2: Effect of polarization in SAR images

This test case explores the impact of polarized EM waves by creating SAR images under three different polarization modes. The third column of Table 4 contains the tuning parameters of modelled SAR images in Figure 12. Figures 12(a–c) indicate the VV, HH, and VH polarized images, respectively. The VV polarized SAR image has a brighter response to rough surfaces than HH, and VH polarized images, as seen in

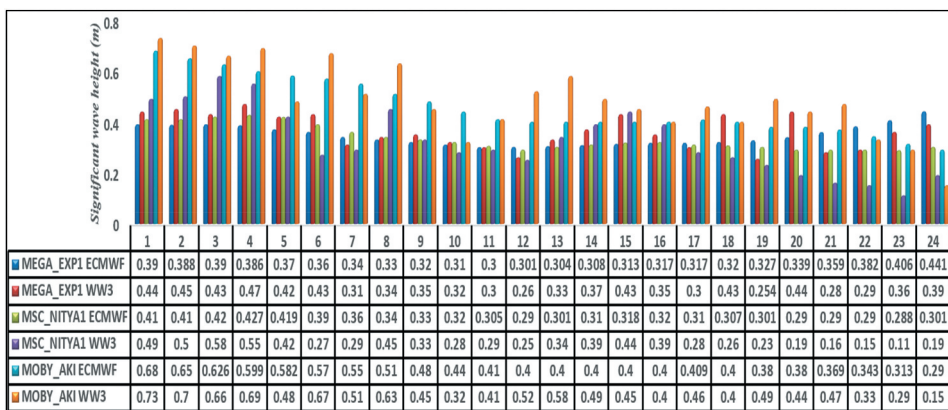


Figure 10. Significant wave height comparison between WW3 results and ECMWF data on July 6, 2020.

Table 4. Configurations of scanning and hydrodynamic parameters under various test cases.

Parameters	Test cases									
	1	2	3	4	5	6	7	8	9	10
SAR platform	Aircraft –1, Aircraft –2, Space –1, Space –2.	Aircraft –1	Aircraft –1	Aircraft –1	Aircraft –1	Aircraft –1	Aircraft –1	Aircraft –1	Aircraft –1	Aircraft –1
Operating bands	X	X	X, C, and L	X	X	X	X	X	X	X
Polarization	VV	VV, HH, and VH	W	W	W	W	W	W	W	W
Incidence angle	23°	23°	23°	23°, 35°, and 60°	23°	23°	23°	23°	23°	23°
Spatial resolution	1 m	1 m	1 m	1 m	1 m	1 m	1 m	1 m	1 m, 2 m, 5 m, 10 m, 1 m × 5 m, 5 m × 1 m	1 m
No.of.looks	1	1	1	1	1	1	1	1	1	1, 2
Wind speed	2.9 m/s	2.9 m/s	2.9 m/s	2.9 m/s	2.9 m/s, 4 m/s, and 7 m/s	2.9 m/s	2.9 m/s	2.9 m/s	2.9 m/s	2.9 m/s
Wind spectrum	Elfouhaily	Elfouhaily	Elfouhaily	Elfouhaily	Elfouhaily	Elfouhaily	Elfouhaily	Elfouhaily	Elfouhaily	Elfouhaily
Submarine model	Sindhughosh	Sindhughosh	Sindhughosh	Sindhughosh	Sindhughosh	Sindhughosh	Sindhughosh	Sindhughosh	Sindhughosh	Sindhughosh
Moving velocity of submarine	25 knots	25 knots	25 knots	25 knots	25 knots	25, 20, 15, and 10 knots	25 knots	25 knots	25 knots	25 knots
Diving depth of submarine	10 m	10 m	10 m	10 m	10 m	10 m	10 m and 20 m	10 m	10 m	10 m
Moving direction of submarine	0°	0°	0°	0°	0°	0°	0°	0°, 30°, 45°, and 90°	0°	0°

Table 5. SAR imaging platforms.

SAR Platform	Altitude	Moving velocity
Aircraft –1	2.5 km	125 m/s
Aircraft –2	7 km	160 m/s
Space –1 (TerraSAR – X)	514 km	7600 m/s
Space –2 (Sentinel –1)	693 km	7600 m/s

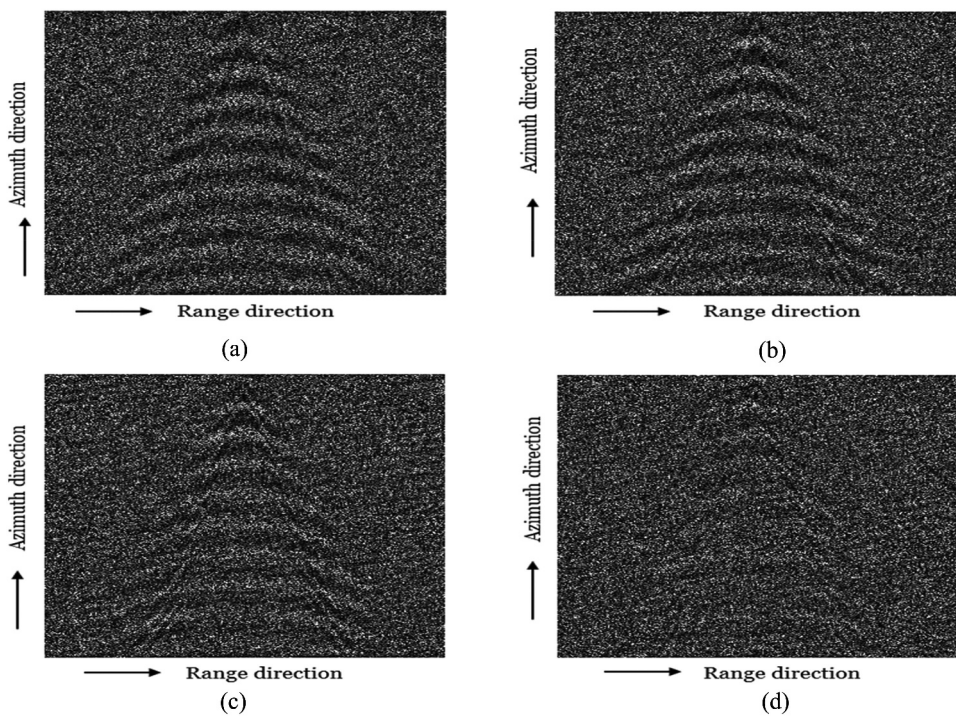


Figure 11. SAR images at various platforms (a) aircraft –1 (b) aircraft –2 (c) space-1 (d) space-2.

Figure 12. Despite the low backscattering intensity in [Figure 12\(b\)](#), it delivers more detailed response (indicated by yellow colour box) than the VV polarized SAR image. This is because the HH polarized SAR image is less sensitive to the speckle noise.

Test case 3: Contribution of operating bands in SAR images

Real-time SAR missions predominantly use the X, C, and L band frequencies. Hence, this paper reveals the outcomes of these three frequency bands. Typically, the SAR system’s operating frequency is set to the band’s centre frequency. Therefore, the functional frequencies of X, C, and L-bands are 10 GHz, 6 GHz, and 1.5 GHz, respectively. The other scanning and hydrodynamic parameters are stated in [Table 4](#). The images in [Figure 13](#) indicate that the visibility of transverse waves increases with frequency, since high-frequency EM waves can capture shorter wavelengths. The findings conclude that the L-band SAR image inadequately depicts all features of the wake pattern compared to C and X bands.

Test case 4: Acquisition of SAR images with various incidence angles

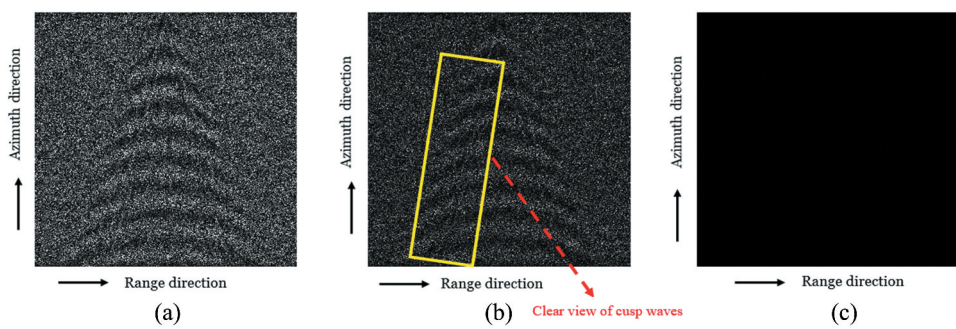


Figure 12. Acquisition of SAR images through (a) VV polarized (b) HH polarized (c) VH polarized EM waves.

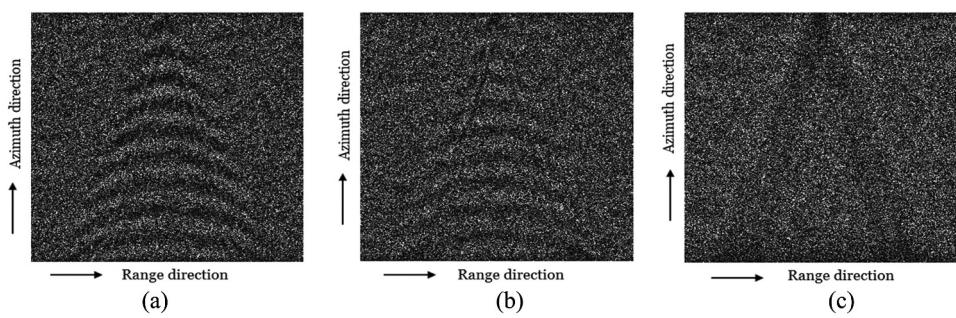


Figure 13. SAR images at different operating bands (a) X-band (b) C-band (c) L-band.

At this case, SAR images are captured at various incidence angles (23° , 35° , and 60°). The rest of the radar and sea parameters are mentioned in fifth column of Table 4. As illustrated in Figure 14, it can be observed that the submarine wake is better imaged at lower incidence angles (23° to 35°). In general, as the incidence angle rises, backscatter intensity drops. This occurs because radar signals traverse a longer distance across the sea surface at elevated angles, which causes greater attenuation. Figure 14(c) complies with this statement.

Test case 5: Repercussion of sea surface roughness on SAR images

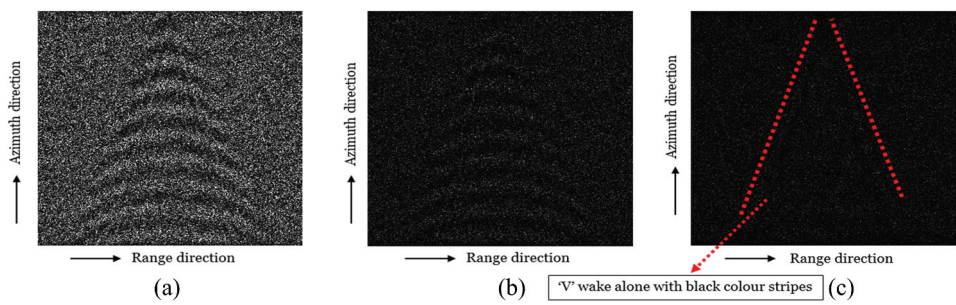


Figure 14. SAR images at distinct incidence angles (a) 23° (b) 35° (c) 60° .

The sea surface roughness is one of the critical factors that obstructs wake characteristics in SAR images. Hence, it is important to investigate the submarine wakes under varying sea state circumstances. The chosen maritime locations are presented in Table 6. Figure 15 considered the radar parameters as listed in Table 4 (6th column). Submarine wake is clearly apparent at wave height of 0.1 m (Figure 15(a)), while at 0.5 m, wake pattern (Figure 15(b)) is intermingled with sea waves. In contrast, it is completely imperceptible at 1.2 m (Figure 15(c)). The images prove that when sea level rises, sea clutter substantially surpasses submarine wakes. Moreover, backscattered signal becomes more intense as surface roughness increases. To demonstrate the significance of precise modelling of sea wave spectra, sea surfaces at locations 2 and 3 have been created using Elfouhaily spectra in lieu of actual spectra at those sites. Figure 16(a) corresponds to location 2, whereas Figure 16(b) is for location 3. Figures 15(b,c) are inconsistent with Figures 16(a) and 16(b) since images in Figure 16 consider only wind wave spectra. This experiment will be further discussed in section 5.3.1 with real-time SAR images.

Test case 6: Impact of submarine's moving velocity on SAR images

In this test instance, SAR images are recorded for the wake patterns of submarines travelling at various velocities. The moving velocities of submarine seen in Figures 17(a–d) are 25 knots, 20 knots, 15 knots, and 10 knots, respectively. The radar parameters are configured as in Table 4 (7th column). Figure 17(a) reveals all features of the submarine manifestation, 'V'-wake with vanished transverse waves are exhibited in Figures 17(b,c) only shows two stripes (highlighted in yellow colour lines), and Figure 17(d) conveys hump details (yellow colour circle). From the illustrations, it is observed that the visibility of the wake pattern increases as moving velocity increases, which confirms the factual theory.

Test case 7: SAR images of submarine wakes at different diving depths

The wake visibility in SAR images also relies on operating depth of submerged vessels. To demonstrate this scenario, SAR images are modelled when the submarines operate at

Table 6. Modelled marine sites.

Locations	Period (Date and Time)	Sea wave height
GOG – MEGA_EXP1	July 6, 2020 at 5:00 pm	0.3 m
ECI – BUOYPOND	September 10, 2017 at 12:00 am	0.5 m
ECI – BUOYPOND	September 15, 2017 at 12:00 am	1.2 m

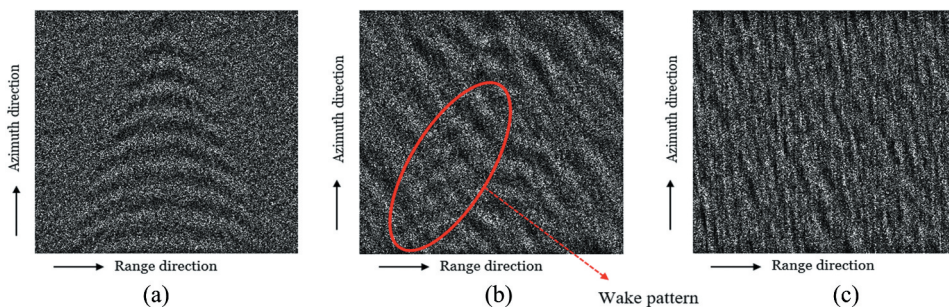


Figure 15. SAR imagery of submarine wakes across three wind wave velocities (a) 2.9 m/s (b) 4 m/s (c) 7 m/s.

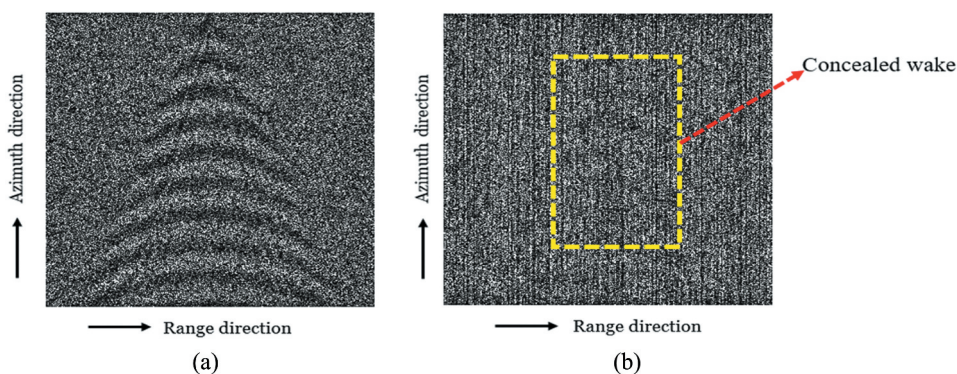


Figure 16. SAR imaging of submarine wakes using elfouhaily wind spectra for the wind speeds of (a) 4 m/s and (b) 7 m/s.

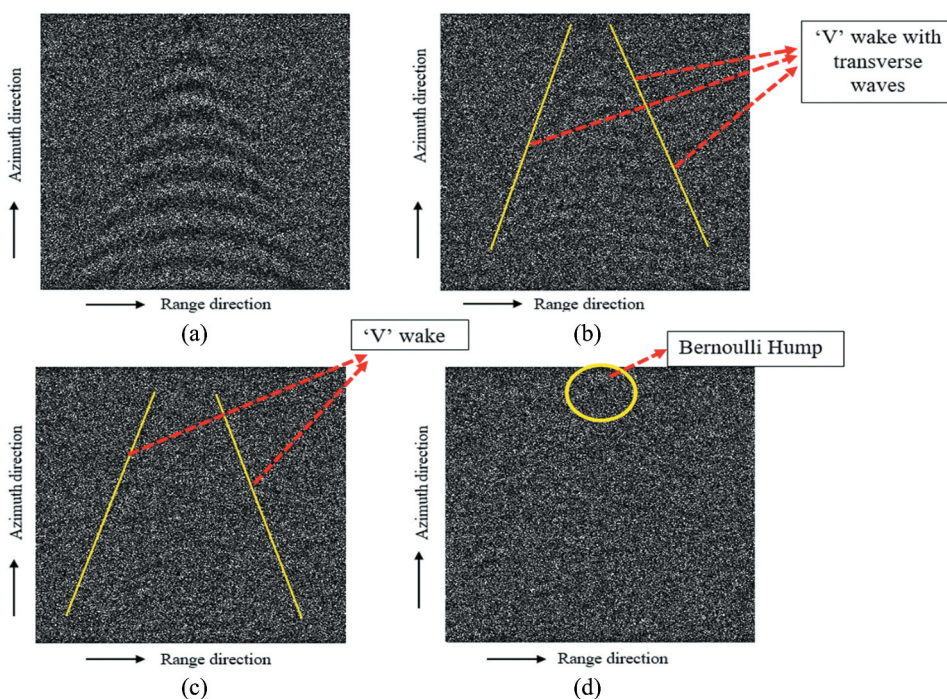


Figure 17. SAR sub wake images at various moving velocities: (a) 25 knots (b) 20 knots (c) 15 knots (d) 10 knots.

depths of 10 m (Figure 18(a)) and 20 m (Figure 18(b)). For that, the SAR imaging parameters are taken from Table 4 (8th column). Based on the figures, it is noted that exposedness of the submarine wake diminishes as the submarine's operational depth increases.

Test case 8: Implication of target's course of movement direction in SAR imagery

The discernibility of the wake pattern is examined through the moving direction of the submarine. The moving trajectory of submarine in Figures 19(a–d) are 0°, 30°, 45°, and 90°.

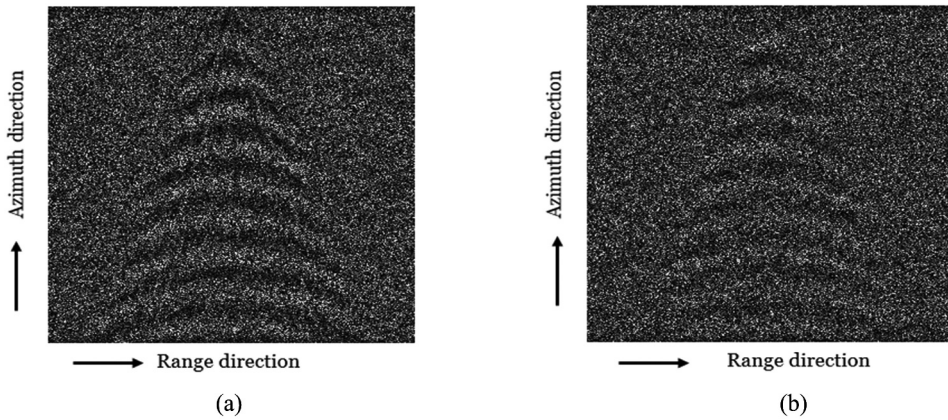


Figure 18. SAR imagery of submarine wakes at the diving depth of (a) 10 m and (b) 20 m with moving velocity of 25 knots.

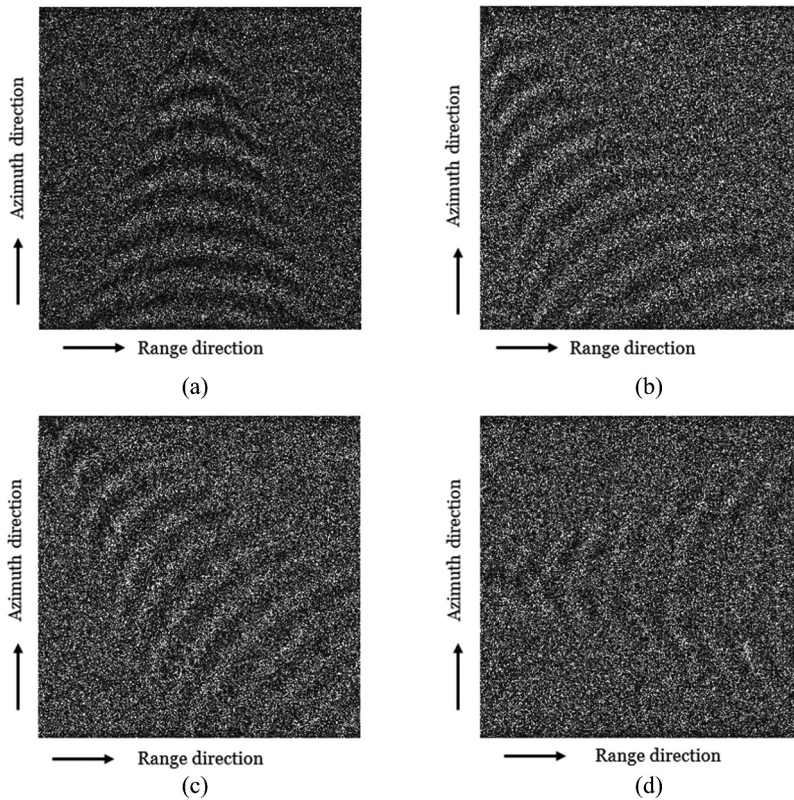


Figure 19. SAR representations of submarine wakes at distinct directions: (a) 0° (b) 30° (c) 45° (d) 90°.

Compared to the other path, at 90° (Figure 19(d)) centre part of the wake has disappeared since the Doppler shift is zero along the line of sight, which complies with the actual SAR principle. This occurrence rigorously substantiates the reliability of proposed model.

In these cases, the ocean environment size is taken as $1000\text{ m} \times 1000\text{ m}$ with 1 m resolution, while the spatial resolution of SAR system is $1\text{ m} \times 1\text{ m}$. Thus, the resultant SAR images have a dimension of $1000\text{ m} \times 1000\text{ m}$. In general, the 1 m spatial resolution is the highest feasible resolution for any real-time SAR system. The spatial resolution of space-borne SAR systems varies from 5 m to 25 m . Thus, the authors introduce test case 9 and examine it using various spatial resolutions to recreate the real-world scenario.

Test case 9: Influence of spatial resolution on SAR images

The impact of spatial resolution of the SAR system is exemplified in [Figures 20 and 21](#). The spatial resolution of the SAR images in [Figure 20](#) remains the same across range and flight directions, while the resolution in [Figure 21](#) varies along these axes. Besides, the remaining radar parameters are pointed out in the 10th column of [Table 4](#). [Figures 20\(a–d\)](#) have spatial resolutions of 1 m , 2 m , 5 m , and 10 m , relatively. As a result, the dimensions of [Figures 20\(a–d\)](#) are $1000\text{ m} \times 1000\text{ m}$, $500\text{ m} \times 500\text{ m}$, $200\text{ m} \times 200\text{ m}$, and $100\text{ m} \times 100\text{ m}$. In compliance with the SAR images in [Figure 20](#), it is perceived that the quality of the SAR image degrades as its spatial resolution decreases. Further, [Figures 20\(b–d\)](#) are darker than [Figure 20\(a\)](#), implying that the strength of backscattering diminishes as the spatial resolution decreases.

Then, the spatial resolutions of [Figures 21\(a\) and 20\(b\)](#) are $5\text{ m} \times 1\text{ m}$ and $1\text{ m} \times 5\text{ m}$. Hence, [Figure 21\(a\)](#) has a size of $200\text{ m} \times 1000\text{ m}$, whereas $1000\text{ m} \times 200\text{ m}$ is the resultant dimension of [Figure 21\(b\)](#). [Figure 21\(a\)](#) is compressed along range axis, and [Figure 21\(b\)](#) is

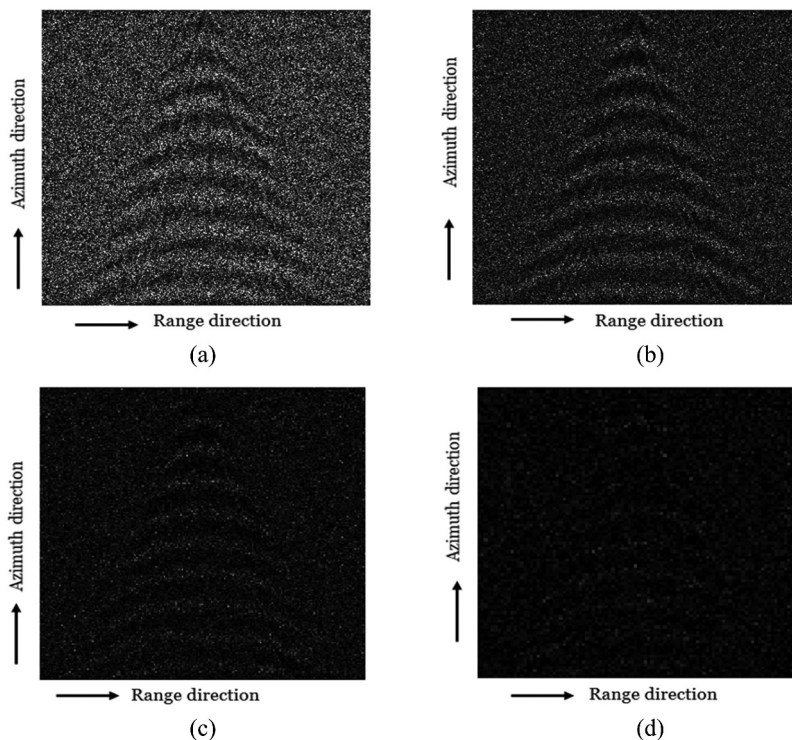


Figure 20. SAR images at various spatial resolutions (a) $1\text{ m} \times 1\text{ m}$ (b) $2\text{ m} \times 2\text{ m}$ (c) $5\text{ m} \times 5\text{ m}$ (d) $10\text{ m} \times 10\text{ m}$.

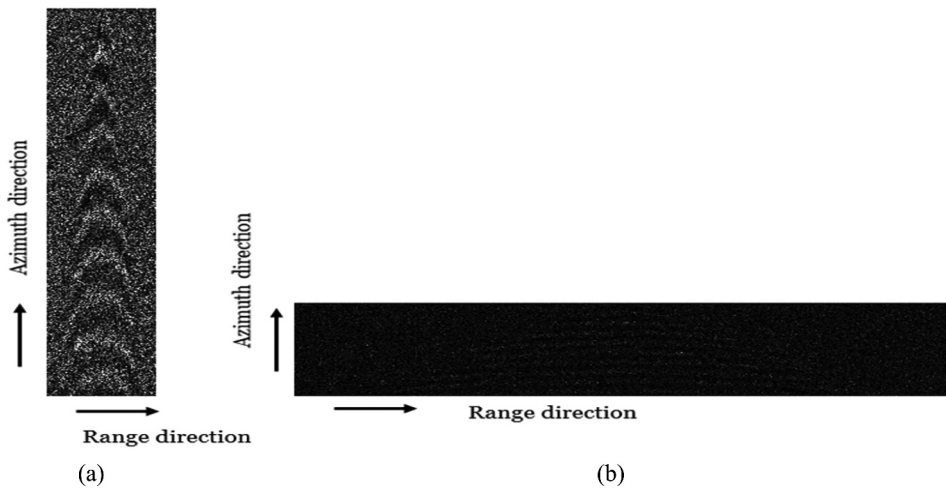


Figure 21. SAR images at different range and azimuth resolutions (a) $5\text{ m} \times 1\text{ m}$ (b) $1\text{ m} \times 5\text{ m}$.

elongated over that same axis since the range resolution is high in [Figure 21\(b\)](#) but low in [Figure 21\(a\)](#). The SAR images in [Figure 20](#) and [Figure 21](#) confirm that the backscattering intensity reduces when there is a degradation in azimuth resolution.

Test case 10: Relevance of multi-look image manipulation

[Figure 22\(a\)](#) and [22\(b\)](#) show the contrasting implications of single-look and multi-look processing on the SAR images. In this case, Kaiser Kernel is generated for 5 points with the shape parameter as 10 to attenuate unwanted frequency components within a multi-look processing. [Figure 22\(a\)](#) indicates the intensity response of a single-look SAR image with a resolution of $5\text{ m} \times 5\text{ m}$. The same image after two-look processing is illustrated in [Figure 22\(b\)](#). It slightly improves the quality of the image. The 'V'-wake in [Figure 22\(b\)](#) is more apparent than single-look image. As in [Figure 22\(b\)](#), the two-look SAR image also reduces the effect of speckle noise.

The above test cases substantiate that radar and hydrodynamic parameters collectively affect the appearance of wake patterns in SAR images. The hydrodynamic parameters

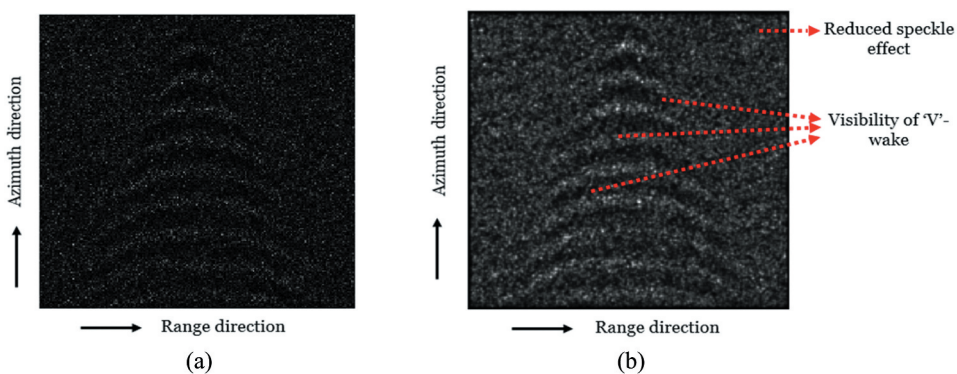


Figure 22. Impact of multi-look processing in SAR imagery (a) single-look (b) two-look.

cannot be adjusted in real-time to generate a discernible wake pattern in SAR images. However, one can design the SAR imaging system with appropriate scanning parameters. The following findings are observed from the ten test cases.

- (1) SAR imaging using X-band yields good outcomes compared to other bands.
- (2) The SAR system can capture observable wake patterns at low incidence angles.
- (3) EM waves that are HH-polarized are less susceptible to the speckle noise than those that are VV-polarized.
- (4) The airborne platforms provide better results than space-borne systems. However, for global coverage, space-borne radars are preferred to airborne ones. The satellite radars at lower altitudes (TerraSAR-X) can produce good-quality SAR images.
- (5) Multi-look processing improves the quality of low-resolution SAR images by enhancing the radiometric properties of the image.
- (6) Further, backscattered intensity of the SAR image depends on following parameters: polarization, look angles, roughness of the sea surface, and azimuth resolution. The backscattering intensity is directly proportional to sea surface roughness and azimuth resolution and is indirectly proportional to look angles. The other modelling parameters (operating band, moving platform, submarine moving velocity, direction, and diving depth) affect the wake pattern legibility but not radar backscattered intensity.

5.3. Verification of proposed SAR imaging system with sentinel-1 imagery

The proposed SAR imaging framework is evaluated under two distinct circumstances. Firstly, the modelled SAR images of ocean surfaces are evaluated through Sentinel-1 imagery, and then the second assessment is conducted on SAR images of wake patterns. The first case considers study area 1, while study area 2 is selected for the second case. The SAR image validation involves both qualitative and quantitative comparison. The qualitative comparison is accomplished through image visuals, pixel value distribution, frequency spectra, wavelet, and curvelet energy distribution. Spatial texture and transform-domain features are employed for quantitative analysis. The spatial texture features encompass grey-level co-occurrence matrix (GLCM) parameters and histogram distance measures, whereas transform-domain features include spectral variables, Kurtosis wavelet energy (KWE), and curvelet energy (KCE).

For this intent, six Sentinel-1 SAR images have been collected from the Copernicus website, which include three single-look complex (SLC) images as well as three multi-look SAR vignettes. The Sentinel-1 products and their respective marine scenery are listed in [Table 7](#). The first three images express a simple ocean surface (Z_{sea_wave}) as marine scenery, while the radar viewpoint for the next three images is sea surfaces superimposed with wake patterns. The last three SAR vignettes are derived from two ground range detected (GRD) products. The GRD products contain both amplitude and intensity responses of SAR images. Due to the confined spatial resolution, the resultant images in the GRD-level products utilized multi-look processing. [Table 9](#) presents the SAR ship vignettes and their associated AIS information obtained from these two GRD products being considered in the WW3 simulation.

Table 7. SAR image ids and respective scene consideration for simulation.

SAR images	SAR image id	Regarding the spectrum		Consideration of wake pattern
		Sentinel-1+ Eifouhaily	WW3 + Eifouhaily	
SAR image #1	S1A-WV-SLC-1SSV-20170710T012003-20170710T013558-017402-01D122-E87B-001	✓	-	-
SAR image #2	S1A-WV-SLC-1SSV-20170905T005739-20170905T011758-018233-01EA70-C22A-001	-	✓	-
SAR image #3	S1A-WV-SLC-1SSV-20171029T000558-20171029T002843-019020-02028A-2593-001	-	✓	-
SAR vignette #1	S1A_IW_GRDH_1SDV_20200706T171436_20200706T171501_033337_03DCC6_1122	-	✓	✓
SAR vignette #2		-	✓	✓
SAR vignette #3	S1A_IW_GRDH_1SDV_20200706T171411_20200706T171436_033337_03DCC6_3302	-	✓	✓

Table 8. AIS information for the SAR vignettes.

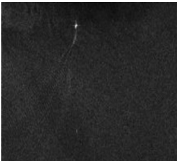
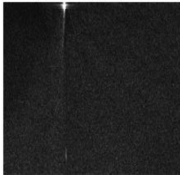


S.No	Ship details	Corresponding Images
1.	Name: MEGA EXPRESS Length: 176 m Width: 25 m Direction: 133° Velocity: 27.4 knots Lat – Long: 43.04° – 9.48°	
2.	Name: MSC NITYA B Length: 330 m Width: 48 m Direction: 169° Velocity: 12.2 knots Lat – Long: 43.01° – 9.59°	
3.	Name: MOBY AKI Length: 175 m Width: 28 m Direction: 52° Velocity: 26.2 knots Lat – Long: 41.72° – 11.12°	
4.	Name: LA SUPERBA Length: 211 m Width: 30 m Direction: 161° Velocity: 22.6 knots Lat – Long: 43.73° – 9.24°	

Table 9. Modelling parameters for SAR image simulation.

Modelling parameters	SAR image #1	SAR image #2	SAR image #3
Platform altitude	693 km	693 km	693 km
Platform moving velocity	7600 m/s	7600 m/s	7600 m/s
EM signal band	C – band	C – band	C – band
Angle of incidence	24.26°	24.27°	24.31°
Polarization of the signal	VV	VV	VV
Spatial resolution	4 m × 4 m	4 m × 4 m	4 m × 4 m
No.of.looks	1	1	1
Scene size	2000 m × 2000 m	2000 m × 2000 m	2000 m × 2000 m
Wind speed	7.14 m/s	5.94 m/s	5.44 m/s
Wind direction	81.67°	132.35°	244.68°
Wave spectrum	Swell: Sentinel-1 (s1a-wv1-ocn-vv-20170710t012003-20170710t012006-017402-01d122-001.nc) Wind: Elfouhaily spectrum	Swell: WW3 spectrum at SAR1W11 Wind: Elfouhaily spectrum	Swell: WW3 spectrum at SAR1W21 Wind: Elfouhaily spectrum
Spectral discretization	Swell – Wave numbers: 0.0056 – 0.2 rad/m (60 bins) Wind – Wave numbers: 0.0056 – 5 rad/m (120 bins) Direction: 0° – 355° (72 bins)		

5.3.1. SAR sea wave verification

The preliminary development of SAR image has been executed using Sentinel-1 swell spectrum to evaluate the effectiveness of the SAR imaging algorithm. This spectrum is obtained from the level 2 product (S1A_WV_OCN_2SSV_20170710T012003_20170710T013558_017402_01D122_F3B9) and was captured on 10 July 2017 in the Arabian Sea (+16.6075, +69.978). Another two images are designed using WW3 swell spectra at SAR1W11 and SAR1W21 locations. Here, the SAR image simulation is based on the parameters in Table 8.

The original and simulated SAR images are visually represented in Figure 23. Figures 23 (b), 23(e), and 23(h) demonstrate that our proposed algorithm effectively models the spatial features of the SAR images. Additionally, Figures 23(c,f,i) illustrate the distribution of pixel values in both actual and simulated SAR images. The greyscale histograms reveal that the intensity of simulated and real-time SAR images follows a negative exponential

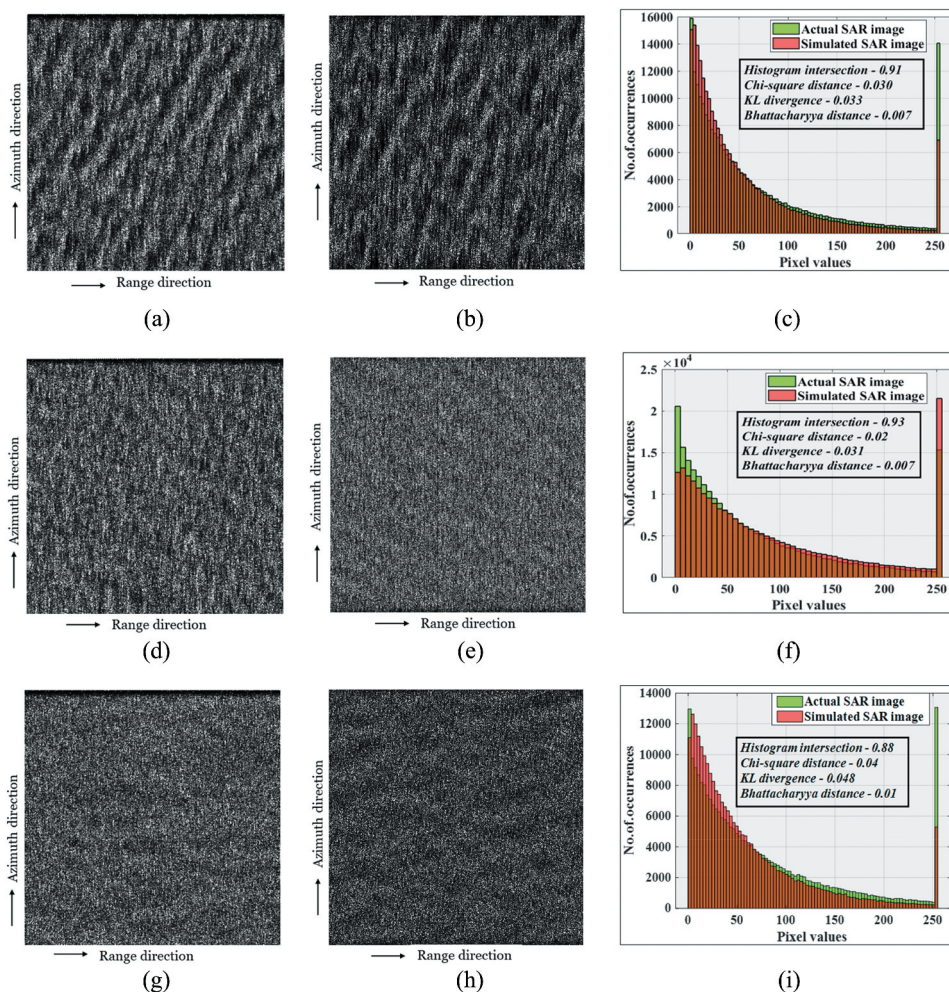


Figure 23. Visual assessment of actual, simulated, and intensity distributions of SAR images for (a–c) SAR image #1 (d–f) SAR image #2 and (g–i) SAR image #3.

spread with significant overlap. This overlapped nature of histograms firmly supports the correlative trend of simulated and actual SAR images. As part of quantitative analysis, [Table 10](#) includes histogram distance measures such as histogram intersection (HI), chi-square distance (CSD), Kullback-Leibler divergence (KLD), and Bhattacharyya distance (BD). HI quantifies overlap between two histograms, while other metrics convey the dissimilarity between the two histograms. The equations used for the computation are detailed in Marín-Reyes, Lorenzo-Navarro, and Castrillón-Santana (2016). The table values (first three entries) imply a higher degree of intersection and minimal dissimilarity between actual and modelled SAR images. However, SAR image #3 exhibits comparatively greater divergent values with less overlap. This may be due to an additional component that is developed in the WW3 swell spectrum, as highlighted in [Figure 11\(d\)](#). The extra component in the SAR image #3 swell spectrum marginally affects the intensity distribution but not the textural characteristics of the ocean surface, as seen in GLCM parameters. Next, the authors estimate the GLCM parameters to statistically describe the texture of sea surfaces. This is achieved by forming GLCM matrices with a displacement vector of [0 1] and 256 grey levels. The renowned GLCM measures such as homogeneity (H), correlation (CR), contrast (C), and energy (E) are calculated (Haralick, Shanmugam, and Dinstein, 2007) and listed in [Table 10](#). Homogeneity refers to the similarity of neighbouring pixels, correlation defines the dependency between pixel pairs, contrast computes the local intensity variations over the whole image, and energy conveys the texture uniformity. As a general rule, rough structures have a greater contrast value, as well as a low degree of homogeneity, correlation, and energy. Due to the rough nature of sea surfaces, the modelled SAR images have higher contrast values and low levels of homogeneity, correlation, and energy metrics. Moreover, SAR image #1 reveals more contrast rating than the other two images because of its rougher surface.

After that, the frequency spectra, wavelet, and curvelet energy distribution of real and synthetic images are compared and exhibited in [Figure 24](#) to ensure the transform-domain relationships. The Fourier-transformed images in [Figures 24\(a\) and 24\(b\)](#) substantiate a significant level of similarity among the spectral characteristics of original and created SAR images. This is also expressed through the peak wavenumber (K_p) and direction (φ_p) estimation from SAR image spectra, as noted in [Table 10](#). This section considers the initial three rows of [Table 10](#). The estimated values show that there will be minimal error in peak wavenumber and directional values extracted from simulated SAR image spectra. In light of the literature (Akbarizadeh 2012, Tirandaz and Akbarizadeh 2015), KWE and KCE are highly sophisticated texture features for SAR images. The KWE measures texture sharpness, while KCE gauges edge sharpness. As in Akbarizadeh (2012), a five-level Haar wavelet is applied to compute coefficients, and the energy values are estimated from approximation coefficients. [Figure 24\(c\)](#) displays the wavelet energy values at each sub-band level of real and simulated SAR images, and [Table 10](#) offers the associated Kurtosis measures. The SAR images are then subjected to fast discrete curvelet transform, and energy distribution is determined for innermost coefficients that approximate the initial image, as outlined in Tirandaz and Akbarizadeh (2015). In [Figure 24\(d\)](#), the curvelet energy levels of actual and simulated SAR images are plotted along each column vector of innermost coefficients, and the respective Kurtosis values are exhibited in [Table 10](#). The wavelet and curvelet energy distribution plots, KWE, and KCE values in

the first three entries of Table 10 strongly indicate that simulated and actual images are comparable. The slight variations in the transform-domain properties have been attributed to the speckle fluctuation between real and modelled SAR images.

Then, SAR image # 3 is selected to demonstrate the special case of test case 5 using real SAR image. Figure 25(a) shows the created SAR image #3 with theoretical wind spectrum, which differs greatly from the actual image in Figure 23(g). Figure 25(b) statistically attests this scenario with intensity distribution. In Figure 25(b), the histogram distance measures between Figures 23(g) and 25(a) are highlighted, emphasizing that the two images have a large amount of dissimilarity with minimal intersection. Thus, accurate sea spectrum extraction is essential while analysing ocean surfaces in SAR images.

5.3.2. Examination of wake patterns in SAR images

The wake formation mechanism remains the same for both ships and submarines (Xue et al. 2021). Despite ships and submarines having different hull shapes, both can create similar wake patterns. The variation is contingent upon submarine's operating depth (Amiri et al. 2019; H. Wu et al. 2019; Xue et al. 2021). This means that the wave disturbances produced by submarines and ships are identical while traversing on the sea surface. Moreover, the SAR images of submarine wakes are inaccessible, so the comparison involves Sentinel-1 SAR imagery of ship wakes and

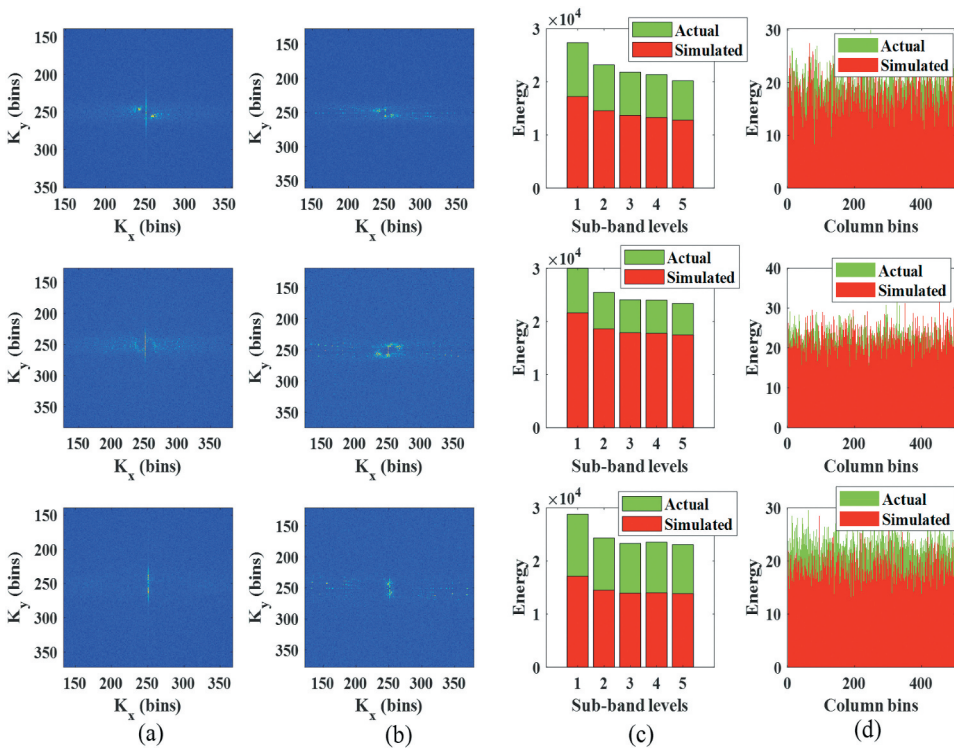


Figure 24. Fourier response of (a) real and (b) modelled images, (c) wavelet energy distribution, (d) curvelet energy distribution of SAR image #1 (top), SAR image #2 (middle), and SAR image #3 (bottom).

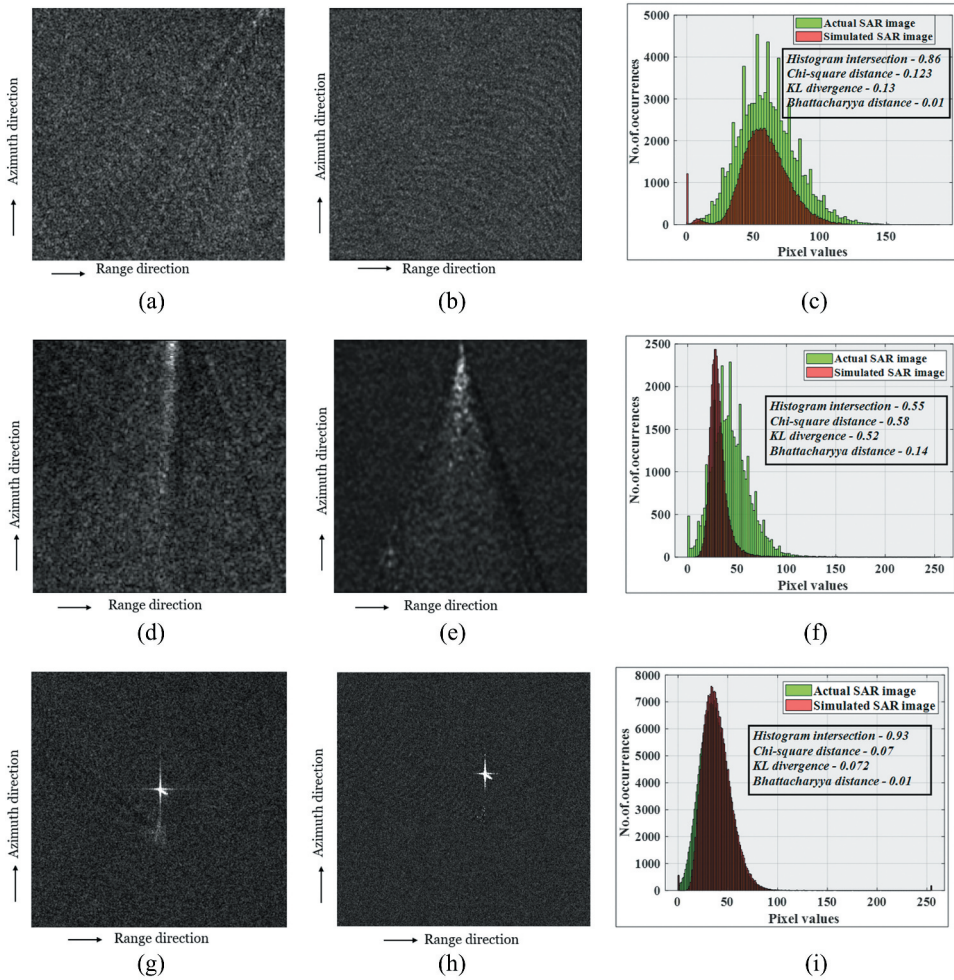


Figure 25. Perceptual evaluation of actual, simulated, and intensity distributions of SAR images for (a–c) SAR vignette #1 (d–f) SAR vignette #2 and (g–i) SAR vignette #3.

modelled SAR images of sea surfaces superimposed with the surface traversal submarine wakes. Here, wake patterns are generated for the mono-hull ship model, utilizing Michell's thin ship theory (Y. Zhang and Jiang 2020). Equations (20)–(23) are applied to model the elevation effects of surface vessels. The simulated wakes are assessed using Kelvin wake heights, which comply with those in the literature (Y. Zhang and Jiang 2020).

$$Z_{surf_wake} = \text{Re} \left(\int_{-90}^{90} A(\varphi) \exp(ik_{cutoff} \sec^2 \varphi (x_{inc} \cos \varphi + y_{inc} \sin \varphi)) d\varphi \right) \quad (20)$$

with,

$$x_{inc} = x \cos \theta_{dir} + y \sin \theta_{dir} \quad (21)$$

$$y_{inc} = -x \sin \theta_{dir} + y \cos \theta_{dir} \quad (22)$$

$$k_{cutoff} = \frac{g}{v^2} \quad (23)$$

where, Z_{surf_wake} is wake elevation of surface vessels, x_{inc}, y_{inc} are inclined x-y coordinates, k_{cutoff} is wave number value at which wake generation commences, v is velocity of the surface vessel (m/s), θ_{dir} indicates moving direction of surface vessels, and $A(\varphi)$ is amplitude, which is derived from the literature (Y. Zhang and Jiang 2020).

The amplitude response of actual and simulated SAR vignettes is illustrated in Figure 26, while the relevant modelling parameters can be found in Table 11. Based on the literature (Xu, Qi, et al. 2024), the ship target is properly placed in Figure 26(h) at the same position as in Figure 26(g) to facilitate an exhaustive comparison. The wake signatures in Figures 26(b,e,h) are compatible with the original SAR vignettes, except for the effect of central turbulent trails. The transverse waves shown in Figures 26(a) and 26(g) are simulated analogously through the proposed algorithm. The right portion of transverse waves is obscured in Figure 26(g), which is also evident in our simulated SAR image. Further, Figure 26(d) illustrates the divergent wake, and Figure 26(e) reproduces the same pattern. Since the amplitude variations of SAR vignettes are examined in this section, the histograms in Figures 26(c,f,i) depict that both actual and simulated images conform to the Rayleigh distribution. As demonstrated by Figures 26(c) and 26(i), the diverged nature of turbulent wake induces minimal discrepancies in the pixel distributions of modelled SAR vignettes. Nonetheless, the amplitude distributions in Figure 26(f) imply that the convergence zone of the turbulent wake pattern leads to the significant deviation of simulated image from original. The last three records of GLCM parameters in Table 10 reflect the aforementioned effects on texture quantification. In comparison to

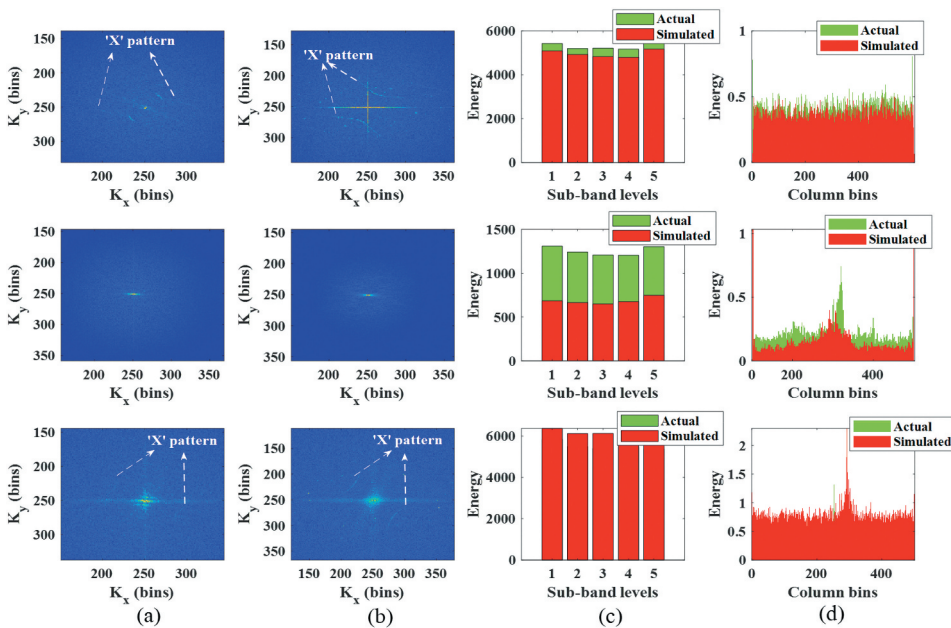


Figure 26. Fourier spectra of (a) real and (b) modelled images, (c) wavelet energy distribution, (d) curvelet energy distribution of SAR vignette #1 (top), SAR vignette #2 (middle), and SAR vignette #3 (bottom).

Table 11. Modelling parameters for SAR image simulation of wake patterns.

Modelling parameters	SAR vignette #1	SAR vignette #2	SAR vignette #3
Platform altitude	693 km	693 km	693 km
Platform moving velocity	7600 m/s	7600 m/s	7600 m/s
EM signal band	C – band	C – band	C – band
Angle of incidence	35.4°	36.2°	42°
Polarization of the signal	VV	VV	VV
Spatial resolution	10 m × 10 m	10 m × 10 m	10 m × 10 m
Scene size	3000 m × 3000 m	3000 m × 3000 m	3000 m × 3000 m
No.of.looks	5 (along track)	5 (along track)	5 (along track)
Wind speed	2.917 m/s	3.15 m/s	4.7 m/s
Wind direction	302.66°	306.85°	296.76°
Submarine parameters	Size: 176 m × 25 m Velocity: 27.4 knots Direction: 133°	Size: 330 m × 48 m Velocity: 12.2 knots Direction: 169°	Size: 175 m × 28 m Velocity: 26.2 knots Direction: 52°
Wave spectrum	Swell: WW3 spectrum at MEGA_EXP1 Wind: Elfouhaily spectrum	Swell: WW3 spectrum at MSC_NITYA1 Wind: Elfouhaily spectrum	Swell: WW3 spectrum at MOBY_AKI Wind: Elfouhaily spectrum
Spectral discretization	Swell – Wave numbers: 0.0056 – 0.2 rad/m (60 bins) Wind – Wave numbers: 0.0056 – 5 rad/m (120 bins) Direction: 0° – 355° (72 bins)		

the very first three observations, these entries have lower contrast and higher correlation, energy, and homogeneity values, confirming that sea surfaces in the SAR vignettes are smoother than the SLC images.

Regarding transform-domain features, the frequency spectra of real and modelled SAR vignettes are presented in [Figures 27\(a,b\)](#), while wavelet and curvelet energy distributions are apparent in [Figures 27\(c,d\)](#). According to the literature (Xue et al. 2020, Arivazhagan et al. 2024), transverse waves of sea vessel wakes manifest an ‘X’ pattern in their Fourier response, which is evident in the first and last rows of [Figure 27](#). The ‘X’ patterns are barely noticeable in real SAR image spectra ([Figure 27\(a\)](#)) because of the turbulent wake effect. The spectral quantities in the bottom three rows of [Table 10](#) also reinforce this trend. Then, the wavelet and curvelet energy distributions of simulated images align closely with actual instances for SAR vignettes #1 and #3. In contrast, they differ tremendously in SAR

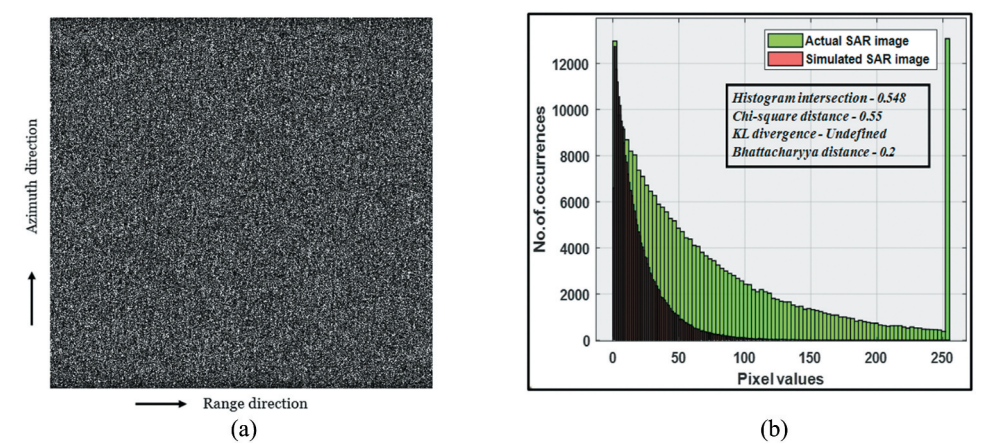


Figure 27. (a) Simulated SAR image #3 with elfouhaily spectrum (b) intensity distribution with actual SAR image #3.

vignette #2. However, there will be minimal deviation in KCE and KWE values, as Kurtosis quantifies the peakedness of the pixel distribution. Additionally, it is noted that the KCE values in the last three entries are higher than those in the first three instances, demonstrating that KCE is a reliable indicator of target presence when compared to KWE.

5.4. Comparative analysis with existing algorithms

In this section, the proposed RVBM algorithm is exhaustively evaluated against SAR wake imaging algorithms like RDA (Jia et al. 2024), omega-K (Xu, Qi, et al. 2024), and standard VB (Rizaev et al. 2022) through visual patterns, quantitative measures, and computational cost. For this analysis, two scenes are taken into consideration: a single-look image (SAR image #1) and a multi-look image (SAR vignette #1). Figure 28 displays the visual comparison results, while Table 13 lists the corresponding quantitative measures. The first row of Figure 28 clearly shows that the velocity bunching effect efficiently captures the swell wave patterns than the RDA and Omega-K algorithms. Because the VB mechanism exploits orbital motion and Doppler shifts of ocean waves, while RDA and omega-K algorithms focus on stationary conditions, which alter the swell wave structure. Values in Table 13 also reflect the corresponding visual result discrepancies. The second row of Figure 28 illustrates how each algorithm responds to the multi-look operation. Typically, multi-look processing is considered a post-processing step in most of the existing SAR imaging algorithms. In contrast, the conventional VB algorithm incorporates the multi-look process internally by using a variable number of looks (N_{look}) and adjusts the influencing factors such as azimuth resolution, integration time, and the orbital motion. However, the adoption of actual multi-look processing is absent in that context. As a result, the multi-look response of VB algorithm adversely affects its visual pattern. The proposed RVBM algorithm tackles this scenario by incorporating sub-image averaging with Kaiser-Bessel weighting function, and the resultant image is comparable with the actual image. The SAR wake images modelled by RDA and omega-K algorithms vary slightly from the real one, as indicated in Table 13. Table 12 displays the computational load of each algorithm computed by (Cumming and Wong 2005). Here, the number of

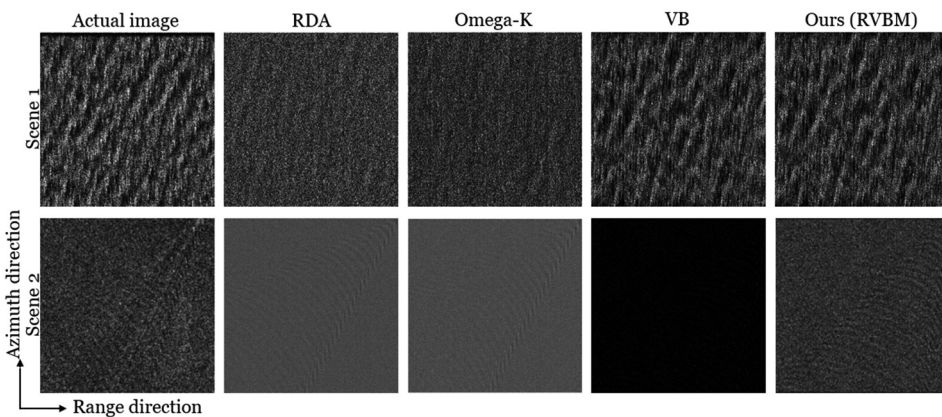


Figure 28. Visual comparisons among various algorithms.

Table 12. Quantitative measures against existing algorithms.

Transform-domain features																																																																																																																							
Spatial texture features										Spectral features					Statistical transform features																																																																																																								
GLCM comparison										Values from actual image spectrum					Values from simulated image spectrum					Statistics from real image transform					Statistics from simulated image transform																																																																																														
Histogram distance measures										Real SAR image					Simulated SAR image					K_p					ϕ_p ($^{\circ}$)					ϕ_p ($^{\circ}$)					KWE					KCE					KCE																																																																										
Methods										HI					CSD					KLD					BD					H					CR					C					E					K_p ($radm^{-1}$)					ϕ_p ($^{\circ}$)					ϕ_p ($^{\circ}$)					KWE					KCE					KCE																																												
Scene 1															RDA					0.86					0.018					0.014					0.003					0.069					0.15					8.56 × 10 ³					1.75 × 10 ⁻⁴					0.058					0.002					5.25 × 10 ³					9.96 × 10 ⁻⁵					0.099					56.3					1.23					85.9					2.59					3.4					3.16					2.8				
															Omega – K					0.87					0.015					0.013					0.002					0.069					0.15					8.56 × 10 ³					1.75 × 10 ⁻⁴					0.06					0.008					6.10 × 10 ³					1.11 × 10 ⁻⁴					0.099					56.3					2.28					85.9					2.59					3.4					3.13					3.18				
															VB					0.91					0.03					0.033					0.007					0.069					0.15					8.56 × 10 ³					1.75 × 10 ⁻⁴					0.063					0.17					6.69 × 10 ³					1.35 × 10 ⁻⁴					0.099					56.3					0.101					52.5					2.59					3.4					2.57					3.12				
															Ours (RVBM)					0.91					0.03					0.033					0.007					0.069					0.15					8.56 × 10 ³					1.75 × 10 ⁻⁴					0.063					0.17					6.69 × 10 ³					1.35 × 10 ⁻⁴					0.099					56.3					0.101					52.5					2.59					3.4					2.57					3.12				
Scene 2															RDA					0.79					0.178					0.165					0.022					0.137					0.62					347.6					2.82 × 10 ⁻⁴					0.21					0.75					452.61					4.59 × 10 ⁻⁴					0.234					43.2					0.273					48.7					2.2					12.7					2.18					16.5				
															Omega – K					0.75					0.215					0.29					0.027					0.137					0.62					347.6					2.82 × 10 ⁻⁴					0.17					0.73					437.23					4.52 × 10 ⁻⁴					0.234					43.2					0.252					49.2					2.2					12.7					2.05					14.8				
															VB					0.24					0.88					0.82					0.48					0.137					0.62					347.6					2.82 × 10 ⁻⁴					0.148					0.011					280.3					6.44 × 10 ⁻⁴					0.234					43.2					1.03					76.2					2.2					12.7					1.055					2.91				
															Ours (RVBM)					0.86					0.123					0.13					0.01					0.137					0.62					347.6					2.82 × 10 ⁻⁴					0.157					0.59					362.78					2.15 × 10 ⁻⁴					0.234					43.2					0.294					45.3					2.2					12.7					1.98					11.4				

Table 13. Comparison of computational loads.

Algorithm	Computational load	
	$N_{look} = 1$	$N_{look} > 1$
RDA	50 MFLOPS	–
Omega-K	49 MFLOPS	–
VB	125 MFLOPS	125 MFLOPS
Ours (RVBM)	125 MFLOPS	$N_{look} * 125$ MFLOPS

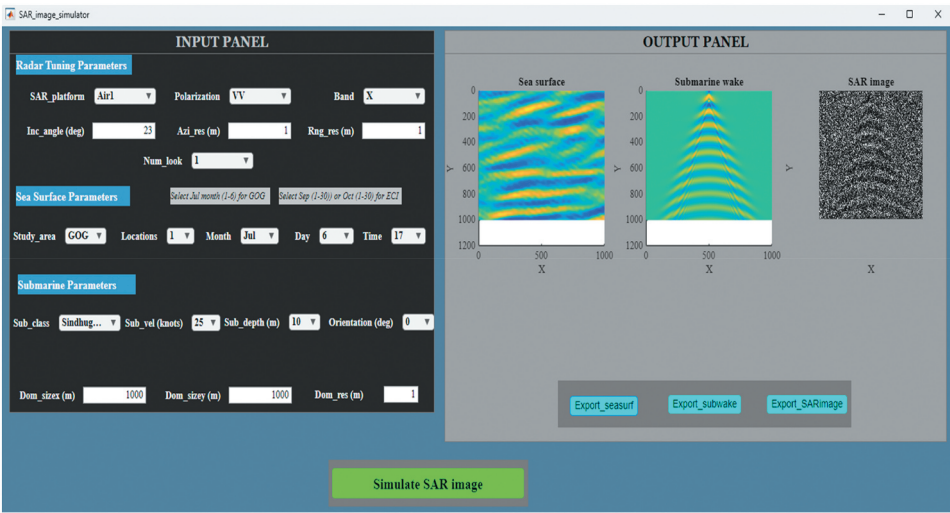


Figure 29. GUI of the proposed SAR imaging system.

range and azimuth lines is set to 500, and interpolation kernel size is taken to be 4. The table values convey that VB and proposed RVBM models require 2.5 times more computation as compared to other models due to the consideration of orbital motion. Regarding multi-look case, RDA and omega-K models didn't handle this internally, whereas the VB model failed to integrate weighted averaging effect. As our proposed model deals with this weighted mean function, it involves N_{look} times of computation for multi-look processing. Overall, the proposed RVBM algorithm yields superior results in simulating both single- and multi-look SAR images, exhibiting a marginal increase in computation relative to existing methods.

5.5. GUI description

Finally, the SAR image simulator is designed with a collection of radar scanning and oceanic parameters, enabling it to perform all the test cases discussed in section 5.2. This GUI interacts with users by leveraging hydrodynamic and electromagnetic parameters through dropdowns, numerical text editors, and push buttons. It consists of a configuration panel and a display panel, as in Figure 29. The input panel contains modelling parameters associated with radar scanning, sea surface, and submarines. In the output panel, display axes project the modelled sea surfaces, submarine wakes, and final

SAR images. The SAR scanning configuration includes a moving platform, resolution, number of looks, operational frequency, polarization, and incidence angle of the electromagnetic waves. Regarding the sea surface, the study area, location, month, day, and time are configurable factors, whereas submarine class, moving velocity, diving depth, and direction are adjustable attributes for wake simulation. Moreover, modelling area of the scene can be altered along x and y axes based on the resolution. Our GUI offers all the aforementioned interfaces with default values that are user-tuneable, as depicted in Figure 29. Table 14 delineates the predefined settings and configurable ranges of all the interfaces employed in this study. This GUI leverages WW3-based modelled sea wave spectra from.nc files to model and display the ocean surfaces of both study areas. It is capable of simulating and visualizing the wake patterns of three classes of Indian submarines, operating at speeds of 30, 25, 20, 15, 10, and 5 knots, and depths of 10, 20, and 30 metres with different orientations. In the meantime, GUI is designed for modelling and exhibiting SAR images under various SAR environments, as discussed in Section 5.2.

Figures 30 denotes the step-by-step realism of the complete GUI usability. The GUI of the SAR image simulator is available as an executable file, compatible with systems that have MATLAB 2024b or later. According to Figures 30(a,b), the main dashboard of the GUI will appear with a splash screen after invoking the executable file. The entire simulation process begins by selecting the push button labelled ‘Simulate SAR image’, which subsequently prompts the sea surface modelling along with a notification, as reflected in Figure 30(c). Upon completion of each stage, the output panel visualizes the modelled outcomes as well as a pop-up message, which is demonstrated through Figure 30(d–f). Then, users are notified upon the detection of invalid inputs and prompted to reconfigure the parameters. Our design interface also allows the users to export the resulting files of ocean surface, wake model, and SAR image by pressing the respective push buttons in the output panel: ‘Export_seasurf’, ‘Export_subwake’, and ‘Export_SARimage’.

Table 14. GUI interfaces and their configurable values.

Modelling parameters			Predefined values	Customizable range
SAR parameters	SAR scanning platform	SAR_platform	Air1	Air1, Air2, Space1, Space 2
	Range resolution	Rng_res	1 m	1 m, 2 m, 5 m, 10 m
	Azimuth resolution	Azi_res	1 m	1 m, 2 m, 5 m, 10 m
	Number of looks	Num_look	1	1, 2, 5
	Polarization of the signal	Polarization	VV	VV, HH
	Operating frequency	Band	X	X, C, L
	Incident angle of the signal	Inc_angle	23°	23°, 35°, 60°
Sea surface	Modelling area	Study_area	GOG	ECL, GOG
	Focal point	Locations	1	1 to 10
	Target month	Month	Jul	Sep, Oct, Jul
	Day of the month	Day	6	1 to 30
	Modelling timestamp	Time	17	1 to 24
Submarine wake	Submarine class	Sub_class	Sindhughosh	Sindhughosh, Shishumar, Kalvari
	Moving velocity	Sub_vel	25 Knots	30, 25, 20, 15, 10 Knots
	Diving depth	Sub_depth	10 m	10 m, 20 m, 30 m
	Moving direction	Orientation	0°	0° to 355°
Scene description	Domain size along x direction	Dom_size_x	1000 m	100 m to 5000 m
	Domain size along y direction	Dom_size_y	1000 m	100 m to 5000 m
	Scene modelling resolution	Dom_res	1 m	1 m

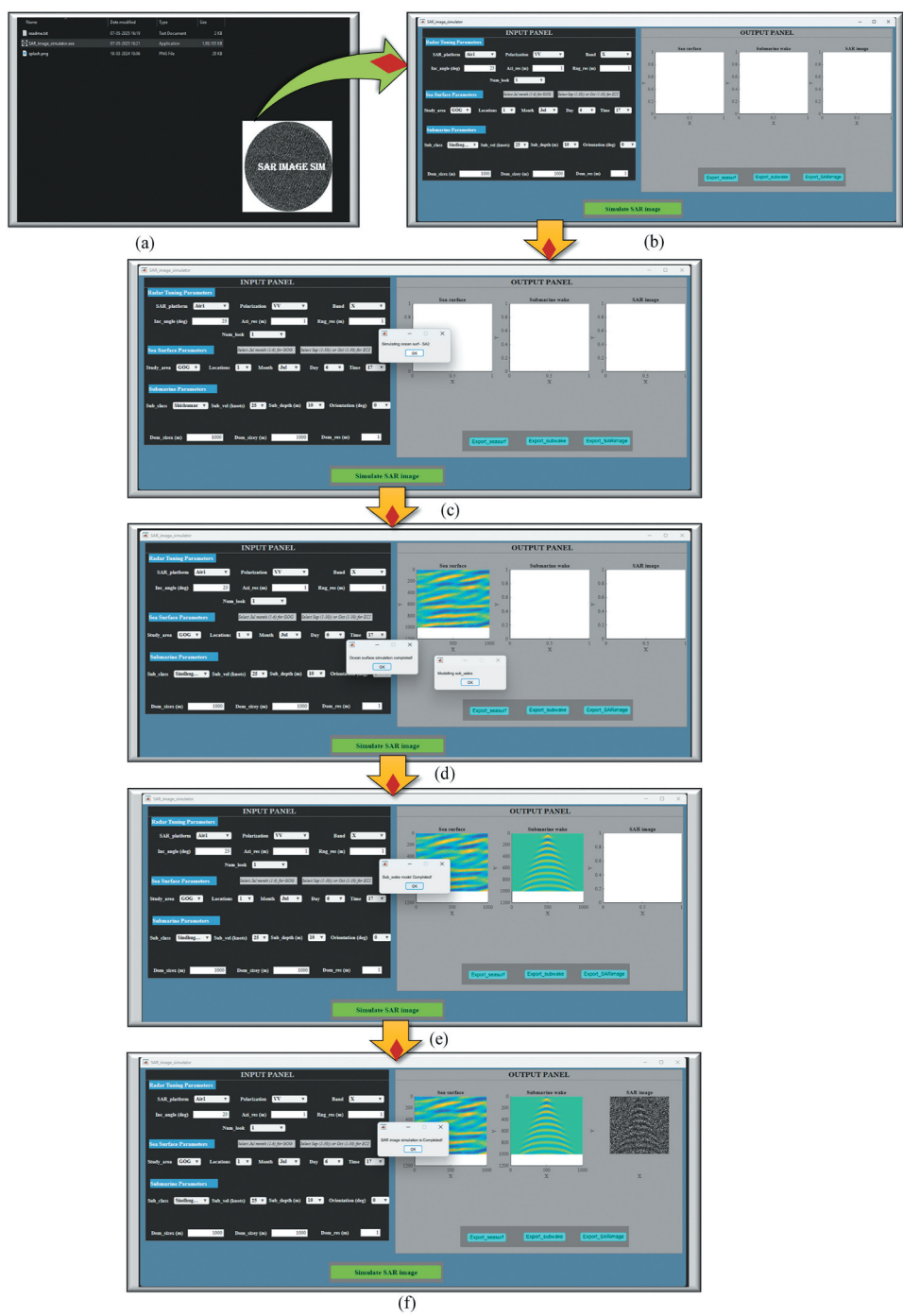


Figure 30. Sequential explanation of GUI functionality (a) execution of SAR image simulator (b) home screen of the GUI (c) triggering of SAR image simulation (d) completion of sea wave modelling (e) end of wake simulation (f) termination of entire simulation process.

6. Conclusion

This work offers an SAR image simulator that leverages a new RVBM methodology to reproduce SAR images of submarine wakes under single- and multi-look processing. The SAR image simulation encompasses WW3 spectra-based sea wave simulation, SPIC-based submarine wake models, and RVBM-based SAR image simulation. The effectiveness of the proposed SAR imaging framework is exhaustively examined through ten different test cases, with the focus on identifying the factors that influence the visibility of the wake pattern. In addition, the credibility of the simulator is verified using real-time SAR images under two distinct oceanic scenarios. The results confirm that the modelled images are comparable with the real-time SAR images. Additionally, the proposed RVBM excels in modelling both single- and multi-look SAR images compared to other algorithms. However, the computational load is around 2.5 times higher relative to other models. Next, the environmental factors such as heavy rainfall, ocean currents, marine life activity, and movement of nearby sea vessels distort the actual wake geometry, which has not been explored in the current analysis. These elements can be inspected in subsequent research. In the future, the dataset constructed from this SAR image simulator can also be used in forthcoming research to establish state-of-art deep learning techniques for detecting and extracting submarine parameters from surface manifestations.

Disclosure statement

No potential conflict of interest was reported by the author(s).

ORCID

M MaryRosaline Tamil Selvi  <http://orcid.org/0000-0002-3349-0793>

References

- Akbarizadeh, G. 2012. "A New Statistical-Based Kurtosis Wavelet Energy Feature for Texture Recognition of SAR Images." *IEEE Transactions on Geoscience & Remote Sensing* 50 (11): 4358–4368. <https://doi.org/10.1109/TGRS.2012.2194787>.
- Alpers, W. 1983. "Monte Carlo Simulations for Studying the Relationship Between Ocean Wave and Synthetic Aperture Radar Image Spectra." *Journal of Geophysical Research Oceans* 88 (C3): 1745–1759. <https://doi.org/10.1029/JC088iC03p01745>.
- Alpers, W., and K. Hasselmann. 1978. "The Two-Frequency Microwave Technique for Measuring Ocean-Wave Spectra from an Airplane or Satellite." *Boundary-Layer Meteorology* 13 (1–4): 215–230. <https://doi.org/10.1007/BF00913873>.
- Alpers, W. R., and C. Bruening. 1986. "On the Relative Importance of Motion-Related Contributions to the SAR Imaging Mechanism of Ocean Surface Waves." *IEEE Transactions on Geoscience & Remote Sensing* 6 (6): 873–885. <https://doi.org/10.1109/TGRS.1986.289702>.
- Alpers, W. R., D. B. Ross, and C. L. Rufenach. 1981. "On the Detectability of Ocean Surface Waves by Real and Synthetic Aperture Radar." *Journal of Geophysical Research Oceans* 86 (C7): 6481–6498. <https://doi.org/10.1029/JC086iC07p06481>.
- Alpers, W., and C. L. Rufenach. 1979. "The Effect of Orbital Motions on Synthetic Aperture Radar Imagery of Ocean Waves." *IEEE Transactions on Antennas & Propagation* 27 (5): 685–690. <https://doi.org/10.1109/TAP.1979.1142163>.

- Amiri, M. M., S. H. Sphaier, M. A. Vitola, and P. T. Esperança. 2019. "Investigation Into the Wave System of a Generic Submarine Moving Along a Straight Path Beneath the Free Surface." *European Journal of Mechanics-B/Fluids* 76:98–114. <https://doi.org/10.1016/j.euromechflu.2019.02.006>.
- Amrutha, M. M., V. S. Kumar, K. G. Sandhya, T. B. Nair, and J. L. Rathod. 2016. "Wave Hindcast Studies Using SWAN Nested in WAVEWATCH iii-Comparison with Measured Nearshore Buoy Data off Karwar, Eastern Arabian Sea." *Ocean Engineering* 119:114–124. <https://doi.org/10.1016/j.oceaneng.2016.04.032>.
- Ardhuin, F., E. Rogers, A. V. Babanin, J. F. Filipot, R. Magne, A. Roland, A. Van Der Westhuysen, et al. 2010. "Semiempirical Dissipation Source Functions for Ocean Waves. Part I: Definition, Calibration, and Validation." *Journal of Physical Oceanography* 40 (9): 1917–1941. <https://doi.org/10.1175/2010JPO4324.1>.
- Arivazhagan, S., M. Shanmuga Sundari, M. Mary Rosaline Tamil Selvi, K. Anilkumar, and A. Vasanathanathan. 2024. "Modeling and Theoretical Exploration of Free Surface Manifestation of Submarines in Presence and Absence of Ocean Waves." *Ocean Engineering* 301:117552. <https://doi.org/10.1016/j.oceaneng.2024.117552>.
- Arnold-Bos, A., A. Khenchaf, and A. Martin. 2007. "Bistatic Radar Imaging of the Marine Environment —Part I: Theoretical Background." *IEEE Transactions on Geoscience & Remote Sensing* 45 (11): 3372–3383. <https://doi.org/10.1109/TGRS.2007.897436>.
- Chen, J., B. Chen, and J. Yang. 2008. "The Turbulent Wake Detection and Beam Estimation of a Ship in SAR Images." In *2008 International Workshop on Education Technology and Training & 2008 International Workshop on Geoscience and Remote Sensing*, Shanghai, China, 1, 230–233. IEEE. <https://doi.org/10.1109/ETTandGRS.2008.157>.
- Cumming, I. G., Y. L. Neo, and F. H. Wong. 2003. "Interpretations of the Omega-K Algorithm and Comparisons with Other Algorithms." *Proceedings of IEEE international geoscience and remote sensing symposium*, Toulouse, France, 3, 1455–1458. IEEE. <https://doi.org/10.1109/IGARSS.2003.1294142>.
- Cumming, I. G., and F. H. Wong. 2005. "Digital Processing of Synthetic Aperture Radar Data." *Artech House* 1 (3): 108–110.
- Del Prete, R., M. D. Graziano, and A. Renga. 2021. "First Results on Wake Detection in SAR Images by Deep Learning." *Remote Sensing* 13 (22): 4573. <https://doi.org/10.3390/rs13224573>.
- Deng, Y., M. Zhang, and L. Wang. 2019. "SAR Image Simulation Analysis of Sea Surface Containing Underwater Object Wake." In *2019 6th Asia-Pacific Conference on Synthetic Aperture Radar (APSAR)*, Xiamen, China, 1–4. IEEE. <https://doi.org/10.1109/APSAR46974.2019.9048433>.
- Ding, K., J. Yang, H. Lin, Z. Wang, D. Wang, X. Wang, K. Ni, and Q. Zhou. 2023. "Towards Real-Time Detection of Ships and Wakes with Lightweight Deep Learning Model in Gaofen-3 SAR Images." *Remote Sensing of Environment* 284:113345. <https://doi.org/10.1016/j.rse.2022.113345>.
- Elfouhaily, T., B. Chapron, K. Katsaros, and D. Vandemark. 1997. "A Unified Directional Spectrum for Long and Short Wind-Driven Waves." *Journal of Geophysical Research Oceans* 102 (C7): 15781–15796. <https://doi.org/10.1029/97JC00467>.
- Ghara, F. M., S. B. Shokouhi, and G. Akbarizadeh. 2022. "A New Technique for Segmentation of the Oil Spills from Synthetic-Aperture Radar Images Using Convolutional Neural Network." *IEEE Journal of Selected Topics in Applied Earth Observations & Remote Sensing* 15:8834–8844. <https://doi.org/10.1109/JSTARS.2022.3213768>.
- Graziano, M. D., and A. Renga. 2021. "Towards Automatic Recognition of Wakes Generated by Dark Vessels in Sentinel-1 Images." *Remote Sensing* 13 (10): 1955. <https://doi.org/10.3390/rs13101955>.
- Haralick, R. M., K. Shanmugam, and I. H. Dinstein. 2007. "Textural Features for Image Classification." *IEEE Transactions on Systems, Man and Cybernetics* 6 (6): 610–621. <https://doi.org/10.1109/TSMC.1973.4309314>.
- Harger, R. O. 1986. "The SAR Image of Short Gravity Waves on a Long Gravity Wave." In *Wave Dynamics and Radio Probing of the Ocean Surface*, edited by O. M. Phillips and K. Hasselmann, 371–392. Boston, MA, US: Springer. https://doi.org/10.1007/978-1-4684-8980-4_26.

- Hasselmann, K., R. K. Raney, W. J. Plant, W. Alpers, R. A. Shuchman, D. R. Lyzenga, C. L. Rufenach, and M. J. Tucker. 1985. "Theory of Synthetic Aperture Radar Ocean Imaging: A MARSEN View." *Journal of Geophysical Research Oceans* 90 (C3): 4659–4686. <https://doi.org/10.1029/JC090iC03p04659>.
- Henderson F. M., and A. J. Lewis, eds. 1998. "Principles And Applications Of Imaging Radar." In *Manual Of Remote Sensing*, 3rd ed. Vol. 2. US: John Wiley & Sons.
- Holthuijsen, L. H. 2010. *Waves in Oceanic and Coastal Waters*. Cambridge university press.
- Jia, Y., S. Liu, Y. Liu, L. Zhai, Y. Gong, and X. Zhang. 2024. "Echo-Level SAR Imaging Simulation of Wakes Excited by a Submerged Body." *Sensors* 24 (4): 1094. <https://doi.org/10.3390/s24041094>.
- Kamirul, K., O. Pappas, I. G. Rizaev, and A. Achim. 2024. "On the Modelling of Ship Wakes in S-Band SAR Images and an Application to Ship Identification." In *2024 IEEE International Geoscience and Remote Sensing Symposium*, Athens, Greece, 10599–10603. IEEE. <https://doi.org/10.1109/IGARSS53475.2024.10642130>.
- Kasilingam, D. P., and O. H. Shemdin. 1988. "Theory for Synthetic Aperture Radar Imaging of the Ocean Surface: With Application to the Tower Ocean Wave and Radar Dependence Experiment on Focus, Resolution, and Wave Height Spectra." *Journal of Geophysical Research Oceans* 93 (C11): 13837–13848. <https://doi.org/10.1029/JC093iC11p13837>.
- Li, D., Z. Zhao, C. Qi, Y. Huang, Y. Zhao, and Z. Nie. 2019. "An Improved Two-Scale Model for Electromagnetic Backscattering from Sea Surface." *IEEE Geoscience & Remote Sensing Letters* 17 (6): 953–957. <https://doi.org/10.1109/LGRS.2019.2940036>.
- Li, J., L. Wang, M. Zhang, Y. C. Jiao, and G. Liu. 2021. "Ship Velocity Automatic Estimation Method via Two-Dimensional Spectrum Pattern of Kelvin Wakes in SAR Images." *IEEE Journal of Selected Topics in Applied Earth Observations & Remote Sensing* 14:4779–4786. <https://doi.org/10.1109/JSTARS.2021.3076846>.
- Li, Q., Y. Zhang, Y. Wang, Y. Bai, Y. Zhang, and X. Li. 2022. "Numerical Simulation of SAR Image for Sea Surface." *Remote Sensing* 14 (3): 439. <https://doi.org/10.3390/rs14030439>.
- Liu, P., and Y. Q. Jin. 2017. "Simulation of Synthetic Aperture Radar Imaging of Dynamic Wakes of Submerged Body." *IET Radar Sonar & Navigation* 11 (3): 481–489. <https://doi.org/10.1049/iet-rsn.2016.0297>.
- Lyzenga, D. R. 1986. "Numerical Simulation of Synthetic Aperture Radar Image Spectra for Ocean Waves." *IEEE Transactions on Geoscience & Remote Sensing* 6 (6): 863–872. <https://doi.org/10.1109/TGRS.1986.289701>.
- Lyzenga, D. R. 1988. "An Analytic Representation of the Synthetic Aperture Radar Image Spectrum for Ocean Waves." *Journal of Geophysical Research Oceans* 93 (C11): 13859–13865. <https://doi.org/10.1029/JC093iC11p13859>.
- Marín-Reyes, P. A., J. Lorenzo-Navarro, and M. Castrillón-Santana. 2016. "Comparative Study of Histogram Distance Measures for Re-Identification". *arXiv preprint arXiv:1611.08134*. <https://doi.org/10.48550/arXiv.1611.08134>.
- Mentaschi, L., G. Besio, F. Cassola, and A. Mazzino. 2015. "Performance Evaluation of WAVEWATCH III in the Mediterranean Sea." *Ocean Modelling* 90:82–94. <https://doi.org/10.1016/j.ocemod.2015.04.003>.
- Modava, M., G. Akbarizadeh, and M. Soroosh. 2019. "Hierarchical Coastline Detection in SAR Images Based on Spectral-Textural Features and Global-Local Information." *IET Radar Sonar & Navigation* 13 (12): 2183–2195. <https://doi.org/10.1049/iet-rsn.2019.0063>.
- Raney, R. K., H. Runge, R. Bamler, I. G. Cumming, and F. H. Wong. 2002. "Precision SAR Processing Using Chirp Scaling." *IEEE Transactions on Geoscience & Remote Sensing* 32 (4): 786–799. <https://doi.org/10.1109/36.298008>.
- Rigling, B. D., and R. L. Moses. 2004. "Polar Format Algorithm for Bistatic SAR." *IEEE Transactions on Aerospace and Electronic Systems* 40 (4): 1147–1159. <https://doi.org/10.1109/TAES.2004.1386870>.
- Rizaev, I. G., and A. Achim. 2022. "Synthwakesar: A Synthetic SAR Dataset for Deep Learning Classification of Ships at Sea." *Remote Sensing* 14 (16): 3999. <https://doi.org/10.3390/rs14163999>.
- Rizaev, I. G., O. Karakuş, S. J. Hogan, and A. Achim. 2022. "Modeling and SAR Imaging of the Sea Surface: A Review of the State-of-the-Art with Simulations." *ISPRS Journal of Photogrammetry & Remote Sensing* 187:120–140. <https://doi.org/10.1016/j.isprsjprs.2022.02.017>.

- Rufenach, C., and W. Alpers. 2003. "Imaging Ocean Waves by Synthetic Aperture Radars with Long Integration Times." *IEEE Transactions on Antennas & Propagation* 29 (3): 422–428. <https://doi.org/10.1109/TAP.1981.1142610>.
- Samadi, F., G. Akbarizadeh, and H. Kaabi. 2019. "Change Detection in SAR Images Using Deep Belief Network: A New Training Approach Based on Morphological Images." *IET Image Processing* 13 (12): 2255–2264. <https://doi.org/10.1049/iet-ipr.2018.6248>.
- Sharifzadeh, F., G. Akbarizadeh, and Y. Seifi Kavian. 2019. "Ship Classification in SAR Images Using a New Hybrid CNN–MLP Classifier." *The Journal of the Indian Society of Remote Sensing* 47 (4): 551–562. <https://doi.org/10.1007/s12524-018-0891-y>.
- Smith, A. M. 1991. "A New Approach to Range-Doppler SAR Processing." *International Journal of Remote Sensing* 12 (2): 235–251. <https://doi.org/10.1080/01431169108929650>.
- Soran, M. B., K. Amarouche, and A. Akpınar. 2022. "Spatial Calibration of WAVEWATCH III Model Against Satellite Observations Using Different Input and Dissipation Parameterizations in the Black Sea." *Ocean Engineering* 257:111627. <https://doi.org/10.1016/j.oceaneng.2022.111627>.
- Sudharsun, G., A. Ali, A. Mitra, A. Jaiswal, P. Naresh, and H. V. Warrior. 2022. "Free Surface Features of Submarines Moving Underwater: Study of Bernoulli Hump." *Ocean Engineering* 249:110792. <https://doi.org/10.1016/j.oceaneng.2022.110792>.
- Tirandaz, Z., and G. Akbarizadeh. 2015. "A Two-Phase Algorithm Based on Kurtosis Curvelet Energy and Unsupervised Spectral Regression for Segmentation of SAR Images." *IEEE Journal of Selected Topics in Applied Earth Observations & Remote Sensing* 9 (3): 1244–1264. <https://doi.org/10.1109/JSTARS.2015.2492552>.
- Umesh, P. A., and M. R. Behera. 2020. "Performance Evaluation of Input-Dissipation Parameterizations in WAVEWATCH III and Comparison of Wave Hindcast with Nested WAVEWATCH III-SWAN in the Indian Seas." *Ocean Engineering* 202:106959. <https://doi.org/10.1016/j.oceaneng.2020.106959>.
- Valenzuela, G. R. 1978. "Theories for the Interaction of Electromagnetic and Oceanic Waves—A Review." *Boundary-Layer Meteorology* 13 (1): 61–85. <https://doi.org/10.1007/BF00913863>.
- Vitale, S., G. Ferraioli, V. Pascazio, and L. G. Deniz. 2025. "Enhanced Deep Learning SAR Despeckling Networks Based on SAR Assessing Metrics." *IEEE Geoscience and Remote Sensing Letters*. <https://doi.org/10.1109/LGRS.2025.3577907>.
- Wang, H., J. Yang, J. Zhu, L. Ren, Y. Liu, W. Li, and C. Chen. 2021. "Estimation of Significant Wave Heights from ASCAT Scatterometer Data via Deep Learning Network." *Remote Sensing* 13 (2): 195. <https://doi.org/10.3390/rs13020195>.
- Wang, J., L. Guo, Y. Wei, and S. Chai. 2023. "Study on Ship Kelvin Wake Detection in Numerically Simulated SAR Images." *Remote Sensing* 15 (4): 1089. <https://doi.org/10.3390/rs15041089>.
- Wang, L., M. Zhang, and J. Wang. 2020. "Synthetic Aperture Radar Image Simulation of the Internal Waves Excited by a Submerged Object in a Stratified Ocean." *Waves in Random and Complex Media* 30 (1): 177–191. <https://doi.org/10.1080/17455030.2018.1492184>.
- Wang, L., M. Zhang, and L. Wang. 2022. "Coupled Model Simulation of the Internal Wave Wakes Induced by a Submerged Body in SAR Imaging." *Waves in Random and Complex Media* 32 (2): 557–574. <https://doi.org/10.1080/17455030.2020.1785040>.
- Wu, H., J. He, H. Liang, and F. Noblesse. 2019. "Influence of Froude Number and Submergence Depth on Wave Patterns." *European Journal of Mechanics-B/Fluids* 75:258–270. <https://doi.org/10.1016/j.euromechflu.2018.10.018>.
- Wu, S., Y. Wang, Q. Li, Y. Zhang, Y. Bai, and H. Zheng. 2023. "Simulation of Synthetic Aperture Radar Images for Ocean Ship Wakes." *Remote Sensing* 15 (23): 5521. <https://doi.org/10.3390/rs15235521>.
- Xu, C., R. Qi, X. Wang, and M. Tao. 2024. "Instability of Energy Spectrum Disturbance for Ship Turbulent Wakes: SAR Imaging Simulation and Analysis." *Ocean Engineering* 292:116502. <https://doi.org/10.1016/j.oceaneng.2023.116502>.
- Xu, C., and X. Wang. 2024. "Opensarwake: A Large-Scale SAR Dataset for Ship Wake Recognition with a Feature Refinement Oriented Detector." *IEEE Geoscience & Remote Sensing Letters* 21:1–5. <https://doi.org/10.1109/LGRS.2024.3392681>.

- Xue, F., W. Jin, S. Qiu, and J. Yang. 2020. "Wake Features of Moving Submerged Bodies and Motion State Inversion of Submarines." *IEEE Access* 8:12713–12724. <https://doi.org/10.1109/ACCESS.2020.2966005>.
- Xue, F., W. Jin, S. Qiu, and J. Yang. 2021. "Airborne Optical Polarization Imaging for Observation of Submarine Kelvin Wakes on the Sea Surface: Imaging Chain and Simulation." *ISPRS Journal of Photogrammetry & Remote Sensing* 178:136–154. <https://doi.org/10.1016/j.isprsjprs.2021.06.001>.
- Ye, J., Y. Wan, C. Fan, and Y. Dai. 2022. "An Improved Two-Scale Model for Sea Surface Scattering in the Transition Range of Incidence Angles." *IEEE Geoscience & Remote Sensing Letters* 19:1–5. <https://doi.org/10.1109/LGRS.2022.3192318>.
- Ye, X., M. Lin, Q. Song, and Q. Wang. 2020. "The Optimized Small Incidence Angle Setting of a Composite Bragg Scattering Model and Its Application to Sea Surface Wind Speed Retrieval." *IEEE Journal of Selected Topics in Applied Earth Observations & Remote Sensing* 13:1248–1257. <https://doi.org/10.1109/JSTARS.2020.2974660>.
- Yonel, B., E. Mason, and B. Yazici. 2017. "Deep Learning for Passive Synthetic Aperture Radar." *IEEE Journal of Selected Topics in Signal Processing* 12 (1): 90–103. <https://doi.org/10.1109/JSTSP.2017.2784181>.
- Zhang, H., J. Ni, K. Li, Y. Luo, and Q. Zhang. 2023. "Nonspare SAR Scene Imaging Network Based on Sparse Representation and Approximate Observations." *Remote Sensing* 15 (17): 4126. <https://doi.org/10.3390/rs15174126>.
- Zhang, H., J. Ni, S. Xiong, Y. Luo, and Q. Zhang. 2022. "SR-ISTA-Net: Sparse Representation-Based Deep Learning Approach for SAR Imaging." *IEEE Geoscience & Remote Sensing Letters* 19:1–5. <https://doi.org/10.1109/LGRS.2022.3202557>.
- Zhang, Y., and L. Jiang. 2020. "A Novel Data-Driven Scheme for the Ship Wake Identification on the 2-D Dynamic Sea Surface." *IEEE Access* 8:69593–69600. <https://doi.org/10.1109/ACCESS.2020.2986499>.
- Zhang, Z., L. Zhang, J. Wu, and W. Guo. 2024. "Optical and Synthetic Aperture Radar Image Fusion for Ship Detection and Recognition: Current State, Challenges, and Future Prospects." *IEEE Geoscience and Remote Sensing Magazine* 12 (4): 132–168. <https://doi.org/10.1109/MGRS.2024.3404506>.
- Zhao, J., W. Guo, Z. Zhang, and W. Yu. 2019. "A Coupled Convolutional Neural Network for Small and Densely Clustered Ship Detection in SAR Images." *Science China Information Sciences* 62 (4): 42301. <https://doi.org/10.1007/s11432-017-9405-6>.
- Zhao, S., Y. Luo, T. Zhang, W. Guo, Z. Zhang, and J. Ren. 2022. "A Feature Decomposition-Based Method for Automatic Ship Detection Crossing Different Satellite SAR Images." *IEEE Transactions on Geoscience & Remote Sensing* 60:1–15. <https://doi.org/10.1109/TGRS.2022.3201628>.
- Zhao, S., J. Ni, J. Liang, S. Xiong, and Y. Luo. 2021. "End-to-End SAR Deep Learning Imaging Method Based on Sparse Optimization." *Remote Sensing* 13 (21): 4429. <https://doi.org/10.3390/rs13214429>.
- Zhao, Y., C. Ou, H. Tian, B. W. K. Ling, Y. Tian, and Z. Zhang. 2024. "Sparse SAR Imaging Algorithm in Marine Environments Based on Memory-Augmented Deep Unfolding Network." *Remote Sensing* 16 (7): 1289. <https://doi.org/10.3390/rs16071289>.
- Zilman, G., A. Zapolski, and M. Marom. 2014. "On Detectability of a Ship's Kelvin Wake in Simulated SAR Images of Rough Sea Surface." *IEEE Transactions on Geoscience & Remote Sensing* 53 (2): 609–619. <https://doi.org/10.1109/TGRS.2014.2326519>.